The strain sensitivity of myo1b is most clearly illustrated in a plot of k_{det} versus force (Fig. 2B), where it can be seen that k_{det} decreases >75-fold with <2 pN of resisting force. At the low forces experienced by myo1b in the absence of the isometric clamp (<0.2 pN, Fig. 1B), a 1.5-fold decrease in k_{det} is predicted over the unloaded rate (k_{g0}), which is consistent with the values of k_{start} measured from the start-time averages.

The fraction of the total ATPase cycle in which myo1b is bound to actin in a force-bearing state is termed the duty ratio, and the force dependence of the duty ratio can be calculated as

$$\text{duty ratio}(F) = \frac{k_{att}}{k_{att} + k_{det}(F)} \qquad (3)$$

where k_{att} is the rate of entry into the strong binding states. k_{att} cannot be determined directly from the force time courses but can be estimated from the rate of phosphate release ($k_{att} = 0.38 \text{ s}^{-1}$, fig. S3). Myo1b transforms from a low–duty-ratio motor (<0.2) to a high–duty-ratio motor (>0.5) when working against as little as 0.5 pN of force, and it approaches the duty ratio of processive myosins (>0.9) at forces as low as 1.5 pN (Fig. 2B, inset).

We investigated the effect of force on the lifetimes and force amplitudes of the working-stroke substeps. Interactions acquired in the presence of 50 µM ATP were sorted into bins based on the force immediately before detachment, and individual interactions were synchronized at their end times and ensemble-averaged. Transient increases in force due to substeps were observed in the 500 ms before detachment in all force bins (Fig. 3A). Single exponential fits of the time courses yielded rates that decreased with increasing force (Fig. 3B). The force dependence of the rates was fit to the equation

$$k_{end}(F) = k_{end0} e^{-\frac{F \cdot d_{end}}{kT}} \qquad (4)$$

where k_{end0} is the rate of the time course in the absence of force and d_{end} is the distance parameter for the substep (Fig. 3B). The best-fit rate of k_{end0} (22 ± 2.5 s^{-1}) is consistent with the rate of 50 µM ATP binding in the absence of resisting loads ($k_{end} = 24 \text{ s}^{-1}$, Fig. 1C), and the value $d_{end} = 2.5 \pm 0.83$ nm is much smaller than d_{det} (Fig. 2B). Therefore, the ATP binding step is not the force-dependent step that limits the rate of actomyo1b detachment. ADP release is the most likely candidate for the force-dependent transition (Fig. 3C). d_{det} is substantially larger than the size of the substep that correlates with ADP release (3.3 ± 0.35 nm, Fig. 1B), indicating that the force-sensitive transition state is not on a coordinate that is in line with a rigid lever arm rotation (24).

The presence of a substep in the end-time averages in all force bins indicates that actomyo1b detachment did not occur before ADP release, even at forces where the detachment rate is force-insensitive (> 1.5 pN; Fig. 2). The force-independent detachment rate (k_i in Eq. 1) is probably the result of accelerated detachment due to force fluctuations in the system. Decreases in force before the ADP-release substep are observed in the force-binned start- and end-time averages (fig. S4). Thus, when force transiently drops, there is an exponentially higher probability of ADP release (Fig. 2B), which is followed by rapid ATP binding and detachment.

Our results show that myosin I responds to small resisting loads (<2 pN) by dramatically increasing the actin-attachment lifetime more than 75-fold. This impressive tension sensitivity supports models that identify myosin I as the adaptation motor in mechanosensory hair cells (2, 3). More generally, the load-dependent kinetics support a model in which myosin I's function to generate and sustain tension for extended time periods, rather than to rapidly transport cargos (fig. S5). This new understanding of myosin I mechanics allows a more rigorous assignment of this motor's molecular roles in controlling organelle morphology (8) and dynamics (5) in the wide variety of cells types in which it is expressed.

References and Notes
1. J. S. Berg, B. C. Powell, R. E. Cheney, *Mol. Biol. Cell* **12**, 780 (2001).
2. J. R. Holt *et al.*, *Cell* **108**, 371 (2002).
3. C. Batters, M. I. Wallace, L. M. Coluccio, J. E. Molloy, *Philos. Trans. R. Soc. London Ser. B* **359**, 1895 (2004).
4. P. G. Gillespie, J. L. Cyr, *Annu. Rev. Physiol.* **66**, 521 (2004).
5. A. Bose *et al.*, *Nature* **420**, 821 (2002).
6. R. E. McConnell, M. J. Tyska, *J. Cell Biol.* **177**, 671 (2007).
7. D. E. Hokanson, J. M. Laakso, T. Lin, D. Sept, E. M. Ostap, *Mol. Biol. Cell* **17**, 4856 (2006).
8. L. Salas-Cortes *et al.*, *J. Cell Sci.* **118**, 4823 (2005).
9. M. A. Geeves, C. Perreault-Micale, L. M. Coluccio, *J. Biol. Chem.* **275**, 21624 (2000).
10. C. Veigel *et al.*, *Nature* **398**, 530 (1999).
11. J. D. Jontes, E. M. Wilson-Kubalek, R. A. Milligan, *Nature* **378**, 751 (1995).
12. R. F. Siemankowski, M. O. Wiseman, H. D. White, *Proc. Natl. Acad. Sci. U.S.A.* **82**, 658 (1985).
13. J. H. Lewis, T. Lin, D. E. Hokanson, E. M. Ostap, *Biochemistry* **45**, 11589 (2006).
14. C. Veigel, S. Schmitz, F. Wang, J. R. Sellers, *Nat. Cell Biol.* **7**, 861 (2005).
15. J. T. Finer, R. M. Simmons, J. A. Spudich, *Nature* **368**, 113 (1994).
16. T. Lin, N. Tang, E. M. Ostap, *J. Biol. Chem.* **280**, 41562 (2005).
17. See methods in supporting information on *Science* Online.
18. C. Veigel, J. E. Molloy, S. Schmitz, J. Kendrick-Jones, *Nat. Cell Biol.* **5**, 980 (2003).
19. D. M. Warshaw *et al.*, *J. Biol. Chem.* **275**, 37167 (2000).
20. C. Ruppert, R. Kroschewski, M. Bahler, *J. Cell Biol.* **120**, 1393 (1993).
21. Y. Takagi, E. E. Homsher, Y. E. Goldman, H. Shuman, *Biophys. J.* **90**, 1295 (2006).
22. G. I. Bell, *Science* **200**, 618 (1978).
23. D. Altman, H. L. Sweeney, J. A. Spudich, *Cell* **116**, 737 (2004).
24. D. Tsygankov, M. E. Fisher, *Proc. Natl. Acad. Sci. U.S.A.* **104**, 19321 (2007).
25. We thank T. Lin for technical assistance and Y. E. Goldman for helpful discussions. Supported by NIH grants AR051174 (H.S. and E.M.O.) and GM057247 (E.M.O.).

The Spread of Ras Activity Triggered by Activation of a Single Dendritic Spine

Christopher D. Harvey,[1,2]* Ryohei Yasuda,[2,3]*† Haining Zhong,[1,2] Karel Svoboda[1,2]†

In neurons, individual dendritic spines isolate *N*-methyl-D-aspartate (NMDA) receptor–mediated calcium ion (Ca^{2+}) accumulations from the dendrite and other spines. However, the extent to which spines compartmentalize signaling events downstream of Ca^{2+} influx is not known. We combined two-photon fluorescence lifetime imaging with two-photon glutamate uncaging to image the activity of the small guanosine triphosphatase Ras after NMDA receptor activation at individual spines. Induction of long-term potentiation (LTP) triggered robust Ca^{2+}-dependent Ras activation in single spines that decayed in ~5 minutes. Ras activity spread over ~10 micrometers of dendrite and invaded neighboring spines by diffusion. The spread of Ras-dependent signaling was necessary for the local regulation of the threshold for LTP induction. Thus, Ca^{2+}-dependent synaptic signals can spread to couple multiple synapses on short stretches of dendrite.

Dendritic spines, small (<1 µm^3) protrusions emanating from the dendritic shaft, are the sites of most excitatory synapses in the mammalian brain (1). Spines function as biochemical compartments (2, 3) that isolate postsynaptic Ca^{2+} accumulations (4–6). Ca^{2+} influx through synaptic *N*-methyl-D-aspartate (NMDA) receptors (NMDA-Rs) activates a complex sig-

naling network (7), including the small guanosine triphosphatase (GTPase) H-Ras (8–10), to induce long-term potentiation (LTP) of synaptic transmission (11, 12). LTP is input specific (13), suggesting that important Ca^{2+}-dependent signals remain confined to single spines. In contrast, synapses interact through diffusible cytoplasmic factors (14–16). Which signals downstream of NMDA-R–dependent Ca^{2+} influx are restricted to individual spines? To begin to address this question, we imaged the dynamics of Ras activity during the induction of input-specific LTP.

We transfected pyramidal neurons in organotypic hippocampal slices with a fluorescence resonance energy transfer (FRET)–based indicator of Ras activation, FRas-F, consisting of H-Ras tagged with monomeric enhanced green fluorescent protein (mEGFP) and the Ras-binding domain [RBD, R59A (mutation of Arg^{59} to Ala)] of Raf tagged with two monomeric red fluorescent proteins (mRFPs) (Fig. 1A) (17). Upon Ras activation, the affinity between Ras and RBD increases, leading to FRET between the donor and acceptor fluorophores (Fig. 1A) (17–19). FRas-F is rapidly reversible and reports the time course of endogenous Ras activation (17). We imaged FRET by using two-photon fluorescence lifetime imaging (2pFLIM) (17, 20, 21). To quantify Ras activation, we computed the fraction of Ras molecules binding to RBD (binding fraction) (Fig. 1B) (17, 22).

To induce synapse-specific plasticity, we applied a train of two-photon glutamate uncaging pulses (30 pulses at 0.5 Hz) to a single spine in a low concentration (nominally 0 mM) of extracellular Mg^{2+} (13, 16). Each uncaging pulse produced transient changes in the concentration of calcium ([Ca^{2+}]) and NMDA-R–mediated currents (7.3 ± 0.6 pA, corresponding to the opening of about five NMDA-Rs), similar to those triggered by low-frequency synaptic stimulation (fig. S1) (6, 22, 23). Uncaging-evoked [Ca^{2+}] accumulations were restricted mostly to the heads of the stimulated spines (fig. S1, A to E) (22). The uncaging train caused a sustained spine enlargement in the stimulated spine; neighboring spines less than 4 μm away did not change (Fig. 1, C to E) (13, 16). The increase in spine volume was proportional to an enhancement in postsynaptic sensitivity to glutamate, indicating that spine enlargement is a structural correlate of LTP (fig. S2C) (13, 16, 24).

The uncaging train induced robust Ras activation in the stimulated spine (Fig. 1, C, F, and G), which peaked within 1 min after the stimulus and returned to baseline levels within 15 min

(decay time constant of Ras activation, τ_{decay} = 5.6 ± 0.5 min). Ras activation required Ca^{2+} influx through NMDA-Rs (Fig. 1H) (8–10). Ras activation also required the activity of multiple signaling factors; inhibitors of calcium/calmodulin-dependent protein kinase II (CaMKII; 10 μM KN62), phosphoinositide 3-kinase (PI3K; 20 μM LY294002), or protein kinase C (PKC; 1 μM Gö6976) signaling reduced Ras activation (Fig. 1H and fig. S3D) (11, 22, 25). The amplitudes of Ras activation and sustained spine enlargement were correlated (fig. S4A). Expression of a dominant-negative form of FRas-F [Ras S17N (mutation of Ser^{17} to Asn)] or inhibition of extracellular signal–regulated kinase (ERK) activation [mitogen-activated protein (MAPK) kinase (MEK) blocker; 10 μM U0126] reduced the magnitude of sustained spine enlargement (fig. S4F) (22). Ras-ERK activation, therefore, was necessary for the persistent increase in spine volume, confirming the role of Ras signaling in synaptic plasticity (11). CaMKII activity, PKC

signaling, and actin polymerization were also required for spine structural plasticity (fig. S4F) (13, 22).

We next characterized the spatial profile of Ras activation (Figs. 1, F and G, and 2, A and B). After the plasticity-inducing stimulus, Ras activity spread over several micrometers in both directions along the parent dendrite and invaded nearby spines (length constant, $L \approx 11$ μm at 4 min) (Fig. 2B), suggesting that Ras signaling is not synapse specific.

Could the presence of the Ras sensor distort the spatial profile of Ras activity? The mean distance active Ras travels before it is inactivated, L, depends on the effective diffusion coefficient of Ras, D, and the time constant of Ras inactivation, $\tau_{inactivation}$ (22):

$$L \sim \sqrt{D\tau_{inactivation}} \qquad (1)$$

FRas-F expression could increase D and $\tau_{inactivation}$ by saturating Ras scaffolds and Ras inactivators
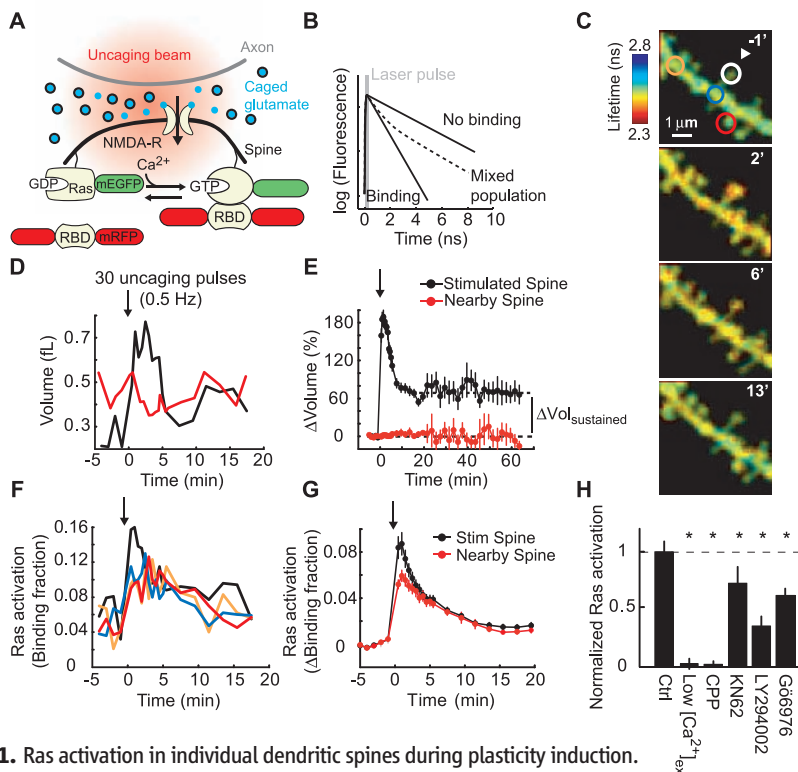

Fig. 1. Ras activation in individual dendritic spines during plasticity induction. (**A**) Experimental geometry. (**B**) Schematic of fluorescence decay curves after pulsed excitation. Slow and fast components correspond to free donor and donor bound to acceptor, respectively. FRET decreases fluorescence lifetime. (**C**) Fluorescence lifetime images of Ras activity. At time = 0, 30 uncaging pulses (0.5 Hz) were applied to the spine marked by the arrowhead in a low concentration (nominally 0 mM) of extracellular Mg^{2+}. "Warmer" colors indicate shorter lifetimes and higher levels of Ras activation. (**D**) Changes in spine volume. Colors correspond to the circles in (C). (**E**) Spine volume changes for the stimulated and nearby (<4 μm) spines (−5 to 20 min: 91 spines; >20 min: 9 spines, mean ± SEM). $\Delta Vol_{sustained}$ is the volume difference between 15.5 and 19.5 min and the baseline volume. (**F**) Ras activation. Colors correspond to the circles in (C). (**G**) Ras activation in the stimulated and nearby spines (82 spines, mean ± SEM). (**H**) Pathways to Ras activation. Ras activation was the average binding fraction at 1 to 3 min minus baseline, normalized to the control condition. Numbers of spines: 82 Ctrl, 11 Low [Ca^{2+}]$_{ex}$ (200 μM), 12 CPP (10 μM), 27 KN62 (10 μM), 20 LY294002 (20 μM), and 23 Gö6976 (1 μM). Error bars indicate mean ± SEM. *P < 0.05 versus control.

[1]Janelia Farm Research Campus, Howard Hughes Medical Institute, Ashburn, VA 20147, USA. [2]Watson School of Biological Sciences, Cold Spring Harbor Laboratory, Cold Spring Harbor, NY 11724, USA. [3]Neurobiology Department, Duke University Medical Center, Durham, NC 27710, USA.

*These authors contributed equally to this work.
†To whom correspondence should be addressed. E-mail: yasuda@neuro.duke.edu, svobodak@janelia.hhmi.org

(GTPase-activating proteins, GAPs), respectively. In addition, RBD competes with GAPs for binding to Ras, further increasing $\tau_{inactivation}$ (*17*). To determine if FRas-F expression increases the spread of Ras activation (fig. S5) (*22*), we modulated FRas-F levels by changing the duration of expression and imaged Ras activation. We quantified FRas-F expression by using post hoc immunofluorescence measurements (fig. S6) (*22*). Ras activation spread along the dendrite even at the lowest FRas-F expression levels tested (~1.5-fold Ras overexpression) (Fig. 2, C and D). Furthermore, the spatial profile of Ras activity was similar across a wide range of FRas-F concentrations (Fig. 2, C and D). FRas-F expression, therefore, did not distort the spatial spread of Ras activation.

We next investigated the mechanisms underlying the spread of Ras activity. Ras mobility could be a major determinant of the spread of Ras activity (Eq. 1). To measure mobility directly, we expressed H-Ras tagged with photoactivatable GFP (paGFP-Ras) (*26*) together with the cytoplasm marker mCherry. After photoactivation in single spines, the spine fluorescence decayed over seconds ($\tau = 4.17 \pm 0.40$ s), similar to the decay rate of membrane-targeted paGFP and less than one-tenth the decay rate of cytosolic paGFP (Fig. 3, A and B) (*3*). These measurements suggest that Ras diffuses relatively freely within the plasma membrane. Constitutively active Ras [Ras G12V (mutation of Gly^{12} to Val)] diffused at a rate similar to that of wild-type Ras (Fig. 3B) and had similar mobility with or without RBD expression (*22*); Ras activation and the binding of RBD to Ras, therefore, did not alter Ras diffusion appreciably. Near physiological temperatures (33°C), Ras mobility was enhanced by a factor of ~2, likely as a result of changes in membrane viscosity (Fig. 3B) (*27*). Within 30 s after photoactivation, more than 90% of the paGFP-Ras G12V fluorescence had decayed from the spine head (Fig. 3D). A similar fraction of membrane-targeted paGFP remained in the spine after 30 s (Fig. 3D). These studies imply that no major immobile fraction of active Ras exists in the spine. Ras overexpression could enhance diffusion by saturating Ras scaffolds (fig. S5A) (*22, 28*). However, the decay time constant and the fraction of fluorescence remaining in the spine at 30 s were independent of paGFP-Ras G12V expression levels (Fig. 3, C and E). These data indicate that active endogenous Ras is highly mobile and does not associate strongly with immobile scaffolds in the spine.

The time constant of Ras inactivation could also modulate the spread of Ras activity (Eq. 1). Because the decay of Ras activity following uncaging stimuli includes both Ras inactivation and diffusion, we instead measured Ras inactivation after brief trains of back-propagating action potentials (bAPs), which activate Ras globally (Fig. 3, F and G) (*17*). Because the length constant of Ras diffusion (~10 μm) (Fig. 2B) is much longer than interspine distances, Ras molecules

Fig. 2. Spatial spread of Ras activity. (**A**) Fluorescence lifetime images of Ras activity. At time = 0, LTP was induced at the spine marked by an arrowhead. (**B**) The spatial spread of Ras activation at different time points. Black circles indicate distances along the dendrite relative to the stimulated spine (gray circle; $n = 11$ cells, mean ± SEM). The solid line shows the fitted profile of Ras activation derived from a one-dimensional diffusion-reaction model (*22*). (**C**) The spatial spread of Ras activation (Ras activation, normalized to peak Ras activation in the stimulated spine, 2 min after stimulus) at various expression levels. (**D**) Normalized Ras activation 3 to 5 μm from the stimulated spine. $r = 0.36$, $P > 0.3$, $n = 8$ cells.
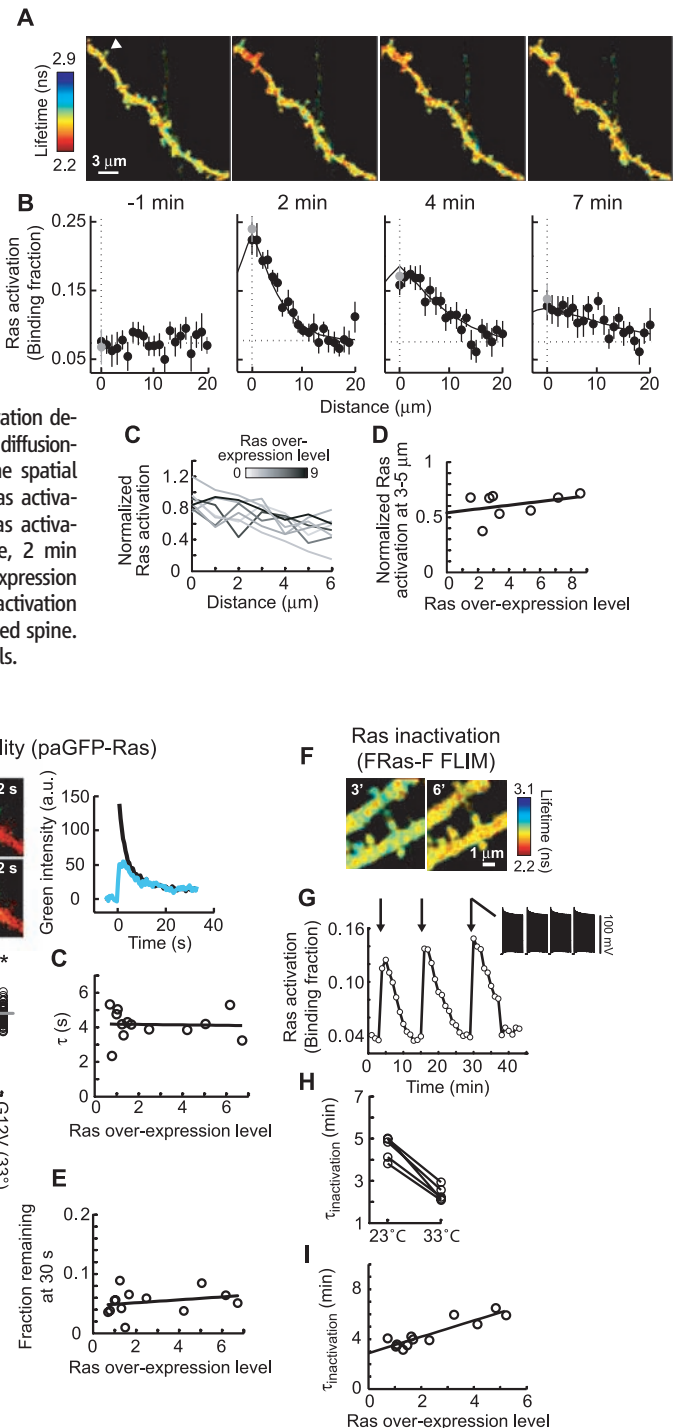

Fig. 3. Ras mobility and the time constant of Ras inactivation. (**A**) Left: Spine before and after photoactivation (green, paGFP-Ras; red, mCherry). Right: Time course of activated paGFP-Ras in the spine (black) and parent dendrite (blue). (**B**) Decay time constants of paGFP fluorescence in the photoactivated spine. Horizontal bars, mean. Numbers of spines: 17 cytosolic, 46 membrane, 21 Ras, 84 Ras G12V, 52 Ras G12V (33°C). *$P < 0.05$ versus paGFP-Ras G12V (23°C). (**C**) Decay time constants of paGFP-Ras G12V fluorescence at varying expression levels. $r = -0.05$, $P > 0.8$, $n = 13$ cells. (**D**) Fraction of paGFP fluorescence remaining in the spine 30 s after photoactivation. Horizontal bars, mean. Number of spines: 46 membrane, 84 Ras G12V. $P > 0.7$. (**E**) Fraction of paGFP-Ras G12V fluorescence remaining in the spine at 30 s at varying expression levels. $r = 0.25$, $P > 0.4$, $n = 13$ cells. (**F**) Fluorescence lifetime images before and after trains of bAPs (40 APs at 83 Hz, repeated four times every 5 s). (**G**) Time course of Ras activation for the experiment shown in (F). Arrows, AP stimuli. (**H**) $\tau_{inactivation}$ at 23°C and 33°C. Ras inactivation was measured at both temperatures in individual cells. $n = 5$ cells, $P < 0.001$. (**I**) Ras inactivation at varying expression levels. $r = 0.8$, $P < 0.01$, slope = 0.6 min per fold overexpression, intercept = 2.9 min. $n = 12$ cells.

activated in both dendrites and spines sample the same population of GAPs, independent of the stimulus. After trains of bAPs, Ras activity decayed over minutes ($\tau_{inactivation}$ = 4.5 ± 0.4 min) (Fig. 3G) (17). Near physiological temperatures (33°C), $\tau_{inactivation}$ was decreased by a factor of ~2 (Fig. 3H). Because this reduction in $\tau_{inactivation}$ was similar to the enhancement of Ras mobility (Fig. 3B), the spread of Ras activity is likely to be relatively independent of temperature (Eq. 1). The duration of Ras activity may be prolonged by FRas-F expression (fig. S5, B and C) (22). However, $\tau_{inactivation}$ was only weakly dependent on FRas-F expression levels (Fig. 3I). Extrapolation to the native case gave $\tau_{inactivation}$ ~ 2.9 min (Fig. 3I). Because RBD and exogenous Ras levels were correlated (r = 0.89, P < 0.001), the estimation of $\tau_{inactivation}$ takes into account the effects of both exogenous Ras and RBD expression. FRas-F therefore increased $\tau_{inactivation}$ by a factor of ~2 and thus the spatial spread by a factor of ~1.5 (Eq. 1). Active Ras in the native case is therefore expected to spread by diffusion over ~10 μm of dendrite, invading 10 to 20 synapses (22).
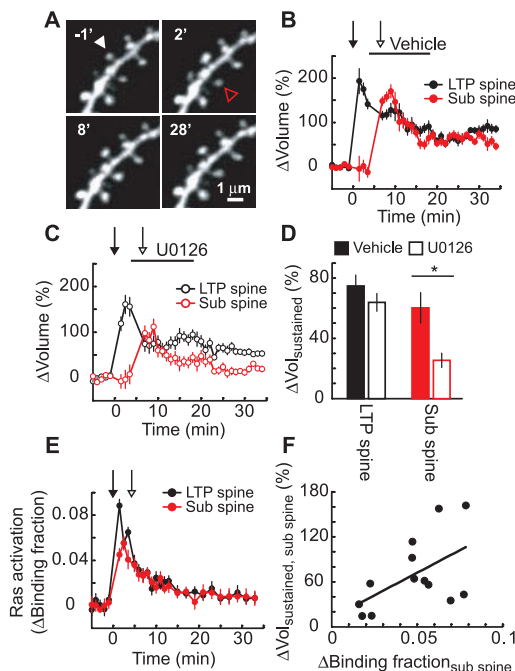
To address whether diffusion of active Ras by itself can quantitatively explain the spread of Ras activity, we modeled the spread of Ras activation using a one-dimensional diffusion-reaction model. In the model, Ras is activated by stationary guanine nucleotide exchange factors (GEFs) in the stimulated spine and is inactivated by GAPs that are distributed homogeneously along the dendrite. By fitting our spatial Ras activity data (Fig. 2B) using a global regression analysis, we obtained estimates of the time constant of GEF activity, τ_{GEF} = 2.0 min, $\tau_{inactivation}$ = 4.5 min, and D = 0.65 μm²/s. These estimates of $\tau_{inactivation}$ and D are identical to the values measured independently (Fig. 3) (22, 29). We conclude that the spread of Ras activation can be explained by the rapid diffusion of active Ras.

What could be the function of the spread of Ras activation? Induction of LTP at a single synapse reduces the threshold for potentiation at neighboring synapses (16). Because the time scales (~5 min) and length scales (~10 μm) of Ras signaling and synaptic crosstalk (16) are identical, we tested whether the spread of Ras activity is critical for the local modulation of the LTP induction threshold.

In a synaptic crosstalk experiment, LTP is induced at one spine (LTP spine) with a train of uncaging pulses; subsequently, a subthreshold uncaging protocol, which by itself is too weak to trigger plasticity (fig. S7C), is sufficient to induce functional and structural plasticity in a neighboring spine (sub spine) (16). If the spread of Ras activity is necessary for crosstalk, Ras-dependent signaling is likely required at a later time in the sub spine as compared to the LTP spine. We induced LTP at a single spine and a short time (3 min) later locally applied a MEK inhibitor (20 μM U0126) to block Ras-ERK signaling; the inhibitor did not decrease the sustained spine-volume change in the LTP spine appreciably (Fig. 4, B to D). We then stimulated a neighboring spine with the subthreshold protocol. The MEK inhibitor substantially reduced the sustained spine enlargement in the sub spine (Fig. 4, B to D), indicating that Ras-dependent signaling is necessary for crosstalk in plasticity.

Ras activity in the sub spine could be caused exclusively by the spread of Ras activity from the LTP spine, but may also include Ras directly activated in the sub spine by the subthreshold protocol. However, the subthreshold protocol alone did not induce detectable Ras activation (fig. S7B). Similarly, in the crosstalk stimulus paradigm, the subthreshold protocol did not trigger additional Ras activation in the sub spine; the decay of Ras activation triggered by the LTP protocol was similar with and without application of the subthreshold protocol (compare Figs. 1G and 4E) (22). Furthermore, the magnitude of Ras activation in the sub spine before the subthreshold protocol, due to the spread of Ras activity, was correlated with the sustained spine enlargement in the sub spine (Fig. 4F). Together, these data indicate that the spread of Ras-dependent signaling is necessary for the local regulation of the LTP induction threshold.

We have shown that Ras signaling after LTP induction spreads along 10 μm of dendrite and invades neighboring spines. The time scale of Ras inactivation was on the order of minutes, as compared with a spine-dendrite diffusional coupling time of seconds. Active Ras can therefore diffuse out of the spine head into the dendrite before inactivating. In contrast, Ca^{2+} is highly compartmentalized because it is extruded much more rapidly (tens of milliseconds) than the diffusional relaxation time between spine and dendrite (hundreds of milliseconds) (6). The diffusional barrier created by the narrow spine neck (2, 3) may be important for rapid signals, such as Ca^{2+}, but is likely less significant for other diffusible signals with longer durations. Synapse-specific plasticity presumably is achieved by signaling molecules that are strongly tethered to postsynaptic scaffolds. The spread of Ca^{2+}-dependent signaling and local functional interactions at the level of plasticity (16) indicate that neighboring synapses are co-regulated. Synapses sharing a short stretch of dendrite may therefore form functional units within individual neurons (30).

Fig. 4. Spread of Ras signaling and synaptic crosstalk. (**A**) Time-lapse images of a GFP-expressing pyramidal neuron in an acute hippocampal brain slice. At time = 0, 30 uncaging pulses (0.5 Hz, 4-ms pulse duration, LTP protocol) were applied to the spine marked by a white arrowhead (LTP spine) in a low concentration (nominally 0 mM) of extracellular Mg^{2+}. At time = 3 min, vehicle (0.1% dimethyl sulfoxide) was pressure applied locally from a glass pipette until time = 17 min. At time = 5.5 min, the subthreshold protocol (30 uncaging pulses, 0.5 Hz, 1-ms pulse duration) was applied to a nearby spine (sub spine, red arrowhead). (**B**) Spine-volume changes in the vehicle condition (11 spines, mean ± SEM). (**C**) Spine-volume changes in the 20 μM U0126 condition (11 spines, mean ± SEM). (**D**) Sustained changes in spine volume. Error bars indicate mean ± SEM. *P < 0.05. (**E**) Ras activation in the LTP and sub spines during the crosstalk paradigm in cultured hippocampal slices. At time = 0, the LTP protocol was applied to the LTP spine, and 3.5 min later, the subthreshold protocol was applied to the sub spine (13 spines, mean ± SEM). (**F**) Relation between Ras activation and the sustained spine enlargement in the sub spine during crosstalk. ΔBinding fraction was measured before the subthreshold protocol (1.5 to 3.5 min after the LTP protocol). r = 0.54, P = 0.05.

References and Notes
1. E. A. Nimchinsky, B. L. Sabatini, K. Svoboda, *Annu. Rev. Physiol.* **64**, 313 (2001).
2. K. Svoboda, D. W. Tank, W. Denk, *Science* **272**, 716 (1996).
3. B. L. Bloodgood, B. L. Sabatini, *Science* **310**, 866 (2005).
4. W. Muller, J. A. Connor, *Nature* **354**, 73 (1991).
5. R. Yuste, W. Denk, *Nature* **375**, 682 (1995).
6. B. L. Sabatini, T. G. Oertner, K. Svoboda, *Neuron* **33**, 439 (2002).
7. M. B. Kennedy, H. C. Beale, H. J. Carlisle, L. R. Washburn, *Nat. Rev. Neurosci.* **6**, 423 (2005).
8. M. J. Kim, A. W. Dunah, Y. T. Wang, M. Sheng, *Neuron* **46**, 745 (2005).
9. X. Tian et al., *EMBO J.* **23**, 1567 (2004).
10. H. Y. Yun, M. Gonzalez-Zulueta, V. L. Dawson, T. M. Dawson, *Proc. Natl. Acad. Sci. U.S.A.* **95**, 5773 (1998).
11. J. J. Zhu, Y. Qin, M. Zhao, L. Van Aelst, R. Malinow, *Cell* **110**, 443 (2002).
12. R. C. Malenka, M. F. Bear, *Neuron* **44**, 5 (2004).
13. M. Matsuzaki, N. Honkura, G. C. Ellis-Davies, H. Kasai, *Nature* **429**, 761 (2004).
14. S. Tsuriel et al., *PLoS Biol.* **4**, e271 (2006).
15. N. W. Gray, R. M. Weimer, I. Bureau, K. Svoboda, *PLoS Biol.* **4**, e370 (2006).
16. C. D. Harvey, K. Svoboda, *Nature* **450**, 1195 (2007).

17. R. Yasuda et al., Nat. Neurosci. 9, 283 (2006).
18. N. Mochizuki et al., Nature 411, 1065 (2001).
19. O. Rocks et al., Science 307, 1746 (2005).
20. D. W. Piston, D. R. Sandison, W. W. Webb, in Time-Resolved Laser Spectroscopy in Biochemistry III, J. R. Lakowicz, Ed. (SPIE, Bellingham, WA, 1992), pp. 379–389.
21. E. Gratton, S. Breusegem, J. Sutin, Q. Ruan, N. Barry, J. Biomed. Opt. 8, 381 (2003).
22. Supporting online material is available on Science Online.
23. E. A. Nimchinsky, R. Yasuda, T. G. Oertner, K. Svoboda, J. Neurosci. 24, 2054 (2004).
24. C. D. Kopec, B. Li, W. Wei, J. Boehm, R. Malinow, J. Neurosci. 26, 2000 (2006).
25. M. Fivaz, S. Bandara, T. Inoue, T. Meyer, Curr. Biol. 18, 44 (2008).
26. G. H. Patterson, J. Lippincott-Schwartz, Science 297, 1873 (2002).
27. E. A. Reits, J. J. Neefjes, Nat. Cell Biol. 3, E145 (2001).
28. H. Niv, O. Gutman, Y. Kloog, Y. I. Henis, J. Cell Biol. 157, 865 (2002).
29. P. H. Lommerse et al., Biophys. J. 86, 609 (2004).
30. A. Losonczy, J. K. Makara, J. C. Magee, Nature 452, 436 (2008).
31. We thank N. Ghitani, B. Burbach, C. Zhang, B. Shields, and H. White for technical assistance; N. Gray for help with immunostaining; L. van Aelst for helpful discussions; and J. Dudman for comments on the manuscript. This work was supported by the Howard Hughes Medical Institute, NIH, a David and Fanny Luke Fellowship (C.D.H.), Burroughs Wellcome Fund (R.Y.), Dana Foundation (R.Y.), National Alliance for Autism Research (R.Y.), National Institute of Mental Health (R.Y.), and National Alliance for Research on Schizophrenia and Depression (H.Z.).

Finite Scale of Spatial Representation in the Hippocampus

Kirsten Brun Kjelstrup,[1] Trygve Solstad,[1] Vegard Heimly Brun,[1] Torkel Hafting,[1] Stefan Leutgeb,[1] Menno P. Witter,[1,2] Edvard I. Moser,[1]* May-Britt Moser[1]

To determine how spatial scale is represented in the pyramidal cell population of the hippocampus, we recorded neural activity at multiple longitudinal levels of this brain area while rats ran back and forth on an 18-meter-long linear track. CA3 cells had well-defined place fields at all levels. The scale of representation increased almost linearly from <1 meter at the dorsal pole to ~10 meters at the ventral pole. The results suggest that the place-cell map includes the entire hippocampus and that environments are represented in the hippocampus at a topographically graded but finite continuum of scales.

Although the basic intrinsic circuitry of the hippocampus is similar along the entire dorsoventral axis of the structure (1), dorsal and ventral regions may not have similar functions. Dorsal and intermediate regions are preferentially connected, via the dorsolateral and intermediate bands of the entorhinal cortex, to visual and somatosensory cortices important for accurate spatial navigation (2–5), and selective lesions in these hippocampal regions can lead to impairments in spatial learning (6–8). Pyramidal cells in these parts of the hippocampus have spatially selective firing fields that reflect the animal's location (9, 10) and jointly form a maplike representation of the environment (10–12). The scale of this representation increases from dorsal to intermediate hippocampus (13, 14), matching the progressive dorsoventral increase in the spacing of grid cells in medial entorhinal cortex, one synapse upstream (15, 16). In contrast, the ventral one-third of the hippocampus has strong connections with a restricted number of interconnected areas of the lateral septum, hypothalamus, and amygdala, both directly and through the ventromedial portions of the entorhinal cortex

(2, 17–19). Selective lesions of the ventral hippocampus affect autonomic and defensive responses but not basic spatial behaviors (20, 21). Collectively, these studies imply a functional division in the hippocampus where the dorsal and intermediate parts are more important for spatial behavior and the ventral part is more relevant for emotional and motivational processes. However, such a division does not rule out the possibility that location is represented at all levels of the hippocampus. Spatial inputs may reach even the most ventral cells via the associational networks of the hippocampus (22, 23) or by way of intrinsic connections between dorsal and ventral parts of the entorhinal cortex (3). To determine whether the ventral hippocampus also has place cells, we compared neural activity at multiple longitudinal levels of CA3 in 21 rats (24). All recording sites were mapped onto the long axis of CA3 (fig. S1). The data were subdivided into three groups based on recording location (dorsal, 7 to 22%; intermediate, 40 to 70%; and ventral, 70 to 100%).

Conventional recording environments may be too small to visualize the most extended hippocampal representations (figs. S2 to S4 and supporting online text). Thus, we tested the animals on an 18-m-long linear track. Well-delineated place fields, defined as spatially stable contiguous regions with firing above 20% of the peak rate, could be found at all longitudinal levels of the hippocampus (Fig. 1 and fig. S5). The representations scaled up between dorsal and ventral recording locations (Fig. 1), from an average place

field size of 0.98 ± 0.03 m in dorsal hippocampus (mean $\pm$ SEM; 111 cells, five rats), to 3.73 ± 0.43 m in intermediate hippocampus (37 cells, three rats), and 5.52 ± 0.54 m in ventral hippocampus (61 cells, four rats). Few fields were longer than 10 m. The relation between recording location and field size was strong (dorsal versus intermediate versus ventral: $F_{2,517} = 86.5$, $P < 0.001$; all pairwise comparisons significant at $P < 0.001$, Bonferroni test). Forty-five per cent of the variance was explained by a linear regression model [$r = 0.67$, $n = 111$, $P < 0.001$; (fig. S6)]. There was a similar increase in the width of the central peak of the spatial autocorrelation function, measured at 20% of the peak value (dorsal, 1.12 ± 0.03 m; intermediate, 3.07 ± 0.19 m; and ventral, 4.10 ± 0.18 m; $F_{2,327} = 179.8$, $P < 0.001$; all pairwise comparisons significant at $P < 0.001$). In this case, 53% of the variance was explained by a linear regression model [$r = 0.73$, 111, $P < 0.001$; (fig. S6; supporting online text)].

The size of individual hippocampal place fields can also be estimated by exploiting the fact that place cells exhibit theta phase precession (25). A place field can be defined as the area between the points on a track where the precession begins and terminates (26). Running on the 18-m track was associated with theta rhythmicity and phase precession at all dorsoventral recording levels in CA3 (81 place cells; Fig. 2 and fig. S7). As the rat crossed the firing field, the firing phase advanced gradually, up to 360°, over successive cycles of the theta rhythm. The strength of precession was estimated for each firing field by rotating the phase by position distribution in steps of 1° across the phase cycle and fitting a linear regression line for each rotation (25, 27). The rotation that gave the largest explained variance was identified. The slope of the regression line at this rotation (phase change per unit of movement) decreased as the field size increased along the long axis of the hippocampus (Fig. 2). In the ventral CA3, the phase advance often occurred over distances as large as 10 m (Fig. 2, right). The mean regression slope changed from $-102° \pm 33°$ per meter in dorsal hippocampus ($t_{62} = 3.1$, $P < 0.005$) to $-18° \pm 9°$ per meter in intermediate and ventral hippocampus ($t_{37} = 2.09$, $P < 0.05$; group difference: $t_{99} = 2.3$, $P < 0.05$; intermediate and ventral cells were combined be-

[1]Kavli Institute for Systems Neuroscience and Centre for the Biology of Memory, Norwegian University of Science and Technology, 7489 Trondheim, Norway. [2]Research Institute Neurosciences, Department of Anatomy and Neurosciences, VU University Medical Center, 1007 MB Amsterdam, Netherlands.

*To whom correspondence should be addressed. E-mail: edvard.moser@ntnu.no

Supporting Online Material for

The Spread of Ras Activity Triggered by Activation of a Single Dendritic Spine

Christopher D. Harvey, Ryohei Yasuda,[*] Haining Zhong, Karel Svoboda[*]

*To whom correspondence should be addressed. E-mail: yasuda@neuro.duke.edu, svobodak@janelia.hhmi.org

This PDF file includes:

Materials and Methods
SOM Text
Figs. S1 to S12
References

Supporting Online Material

Materials and Methods

Preparations

FRas-F consists of monomeric EGFP (mEGFP)-Ras and mRFP-RBD(R59A)-mRFP as described (*1*). GFP-tagged variants of H-Ras are biologically active and show normal subcellular localization, indicating that GFP-Ras participates in endogenous signaling pathways (*2*). RBD contains the R59A mutation to reduce the affinity between GTP-bound Ras and RBD (from $K_D \sim 0.1$ μM to ~ 4 μM) (*3*), allowing GAPs to inactivate Ras rapidly (*1*). mEGFP-Ras was localized mostly to the plasma membrane (Fig. S8), although contributions from mEGFP-Ras on Golgi membranes cannot be excluded (*4-6*). mEGFP-Ras was present in dendritic spines, consistent with endogenous Ras localization (*7, 8*). mRFP-RBD-mRFP was distributed uniformly throughout the cytoplasm. Expression of FRas-F did not affect the cell parameters we measured, including the amplitude of NMDA-R-mediated currents (Fig. S9B), resting membrane potential (*1*), and input resistance (*1*). Also, spine structural plasticity in FRas-F-expressing and GFP-expressing cells showed similar magnitudes, time courses, and pharmacological profiles (compare Figs. 1E, S4F with Fig. S10), suggesting that FRas-F did not perturb the signaling network in the spine. paGFP (*9*) was fused to the N-terminus of H-Ras and H-Ras G12V. For membrane targeting, amino acids 1-40 from MARCKS (*10*) were added to the N-terminus of paGFP.

Hippocampal slice cultures were prepared from postnatal day 6 or 7 rats (*11*), in accordance with the animal care and use guidelines of Cold Spring Harbor Laboratory and Janelia Farm Research Campus. After 5-8 days in culture, cells were transfected by ballistic gene transfer using gold beads coated with a 1:4 molar ratio of mEGFP-Ras:mRFP-RBD(R59A)-mRFP. At the time of transfection, 8 mM $MgCl_2$ (final concentration of 10.8 mM) was added to the culture medium to minimize the effects of Ras over-expression on synaptic efficacy (*12*). Experiments were performed ~ 36 hours after transfection. To decrease expression levels, the duration of expression was reduced to 12-16 hours. The concentrations of exogenous Ras and RBD were correlated across a wide range of expression levels ($r = 0.89$, $P < 0.001$).

Acute hippocampal brain slices (300 μm thick) from Thy1 GFP (line M) or YFP (line H) mice (*13*) were prepared at postnatal days 14-18 (Fig. 4A-D). Slices were cut in gassed (95% O_2 / 5% CO_2), ice-cold cutting solution containing 110 mM choline chloride, 25 mM $NaHCO_3$, 25 mM D-glucose, 2.5 mM KCl, 7 mM $MgCl_2$, 0.5 mM $CaCl_2$, 1.25 mM NaH_2PO_4, 11.5 mM sodium ascorbate and 3 mM sodium pyruvate. Slices were then incubated in artificial cerebral spinal fluid (ACSF) containing 127 mM NaCl, 2.5 mM KCl, 2 mM $CaCl_2$, 1 mM $MgCl_2$, 25 mM $NaHCO_3$, 1.25 mM NaH_2PO_4, 25 mM glucose at 35º C for 30 minutes.

All experiments were performed at room temperature (~ 23º C) in standard ACSF containing 4 mM $CaCl_2$, 0 mM $MgCl_2$, 1 μM TTX, and 2.5 mM MNI-caged-L-glutamate aerated with 95% O_2 and 5% CO_2, unless otherwise noted. For pharmacology studies, slices were incubated with drugs for ~ 30 minutes prior to the start of the experiment.

Imaging and glutamate uncaging

We used a custom-built two-photon microscope with two Ti:sapphire lasers. One laser was tuned to 960 nm to excite both mEGFP-Ras for lifetime measurements and mRFP-RBD(R59A)-mRFP for morphology data. The second laser was tuned to 720 nm for glutamate uncaging. The intensities of each laser beam were controlled independently using electro-optical modulators (Pockels cells, Conoptics). The beams were combined using a beam-splitting cube and passed through the same set of scan mirrors and objective (60x, 0.9 NA, Olympus). 2pFLIM was performed as described (*1*). Custom software (FLIMImage) integrated into ScanImage (*14*) was used to acquire lifetime images. Fluorescence decay curves were measured by comparing the times of laser pulses (80 MHz) detected by a photodiode (FDS010, Thorlabs) and photon pulses from a fast photomultiplier tube (PMT; H7422-40, Hamamatsu) using a time-correlated single photon counting board (SPC-730, Becker-Hickl) (*1, 15*). Fluorescence signals from PMTs (R3896, Hamamatsu) were acquired by ScanImage using a data acquisition board (PCI-6110, National Instruments). The fast epifluorescence PMT was used for 2pFLIM. The summed signal from trans- and epifluorescence PMTs was used for mRFP intensity measurements (*16*), and the signal from a transfluorescence PMT was used for mEGFP

intensity measurements. mEGFP and mRFP fluorescence were separated using a dichroic mirror (565 nm) and bandpass filters (510/70, 635/90; Chroma).

Two-photon glutamate uncaging (*17-23*) was performed in ACSF lacking Mg^{2+} in the presence of MNI-caged-L-glutamate (2.5 mM) and TTX (1 µM). For uncaging pulses 18 mW laser power (720 nm) was delivered to the back focal aperture of the objective for 4 ms, unless noted otherwise. Approximately 20% of this laser power was transmitted through the objective. The uncaging beam was parked at a manually selected location ~ 0.5 µm from the tip of the spine head in the direction away from the parent dendrite. Only spines well separated from both the parent dendrite and neighboring spines were used for experiments.

Photoactivation of paGFP (Fig. 3A-E) was performed in ACSF containing 4 mM Ca^{2+} and 4 mM Mg^{2+}. Cells were transfected with the paGFP construct and mCherry. For paGFP-Ras G12V, co-expression of RBD did not alter the decay-time constant of the paGFP fluorescence in the activated spine ($\tau_{Ras\ G12V\ with\ RBD} = 4.33 \pm 0.07$ seconds, $\tau_{Ras\ G12V\ without\ RBD} = 4.25 \pm 0.15$ seconds, $P > 0.7$). Images were acquired every 128 ms using a laser tuned to 960 or 990 nm. Photoactivation occurred during a single frame by illuminating an ROI with a laser tuned to 810 nm. For each spine, the green fluorescence was normalized to the signal immediately following photoactivation, and the normalized fluorescence was averaged across multiple (≥ 3) trials. Trials were separated by more than 5 minutes to allow the paGFP signal to return to baseline. Photoactivated spines were separated by more than 30 µm to prevent crosstalk of paGFP signals. To determine the decay time constant, τ, the averaged normalized green fluorescence was fit with a single exponential $ae^{-t/b} + c$. Since this time constant, b, also includes the effects of diffusional relaxation between the spine and the dendrite, we then fit the averaged normalized green fluorescence using a single exponential $ae^{-t/\tau}$ over the interval from time = 0 to b (*24*).

Crosstalk in plasticity experiments (Fig. 4) were performed in low (nominally 0 mM) extracellular Mg^{2+} and 1 µM TTX, as described (*23*). Individual uncaging pulses from the LTP and subthreshold protocols had pulse durations of 4 ms and 1 ms, respectively, with 18 mW laser power at the back focal aperture of the objective. The MEK inhibitor (20 µM U0126) and vehicle (0.1% DMSO) were pressure applied from a

glass pipette (~ 5 μm tip diameter) using a Picospritzer. The pipette solution contained ACSF and ~ 10 μM Alexa 594 for visualization. The pipette was positioned ~ 25 μm from the dendrite of interest.

For $[Ca^{2+}]$ imaging, cells were filled with a Ca^{2+}-sensitive green indicator (250 μM Fluo-4FF, G) and a Ca^{2+}-insensitive red dye (10 μM Alexa-594, R; Fig. S1). Images were acquired every 64 ms. $[Ca^{2+}]$ transients were measured as the change in green fluorescence divided by the red fluorescence ($\Delta G/R$), normalized to $(G/R)_{max}$ measured in 10 mM Ca^{2+}.

Electrophysiology

Uncaging-evoked NMDA-R currents and $[Ca^{2+}]$ transients were measured in voltage clamp at –70 mV in ACSF containing low extracellular Mg^{2+} (nominally 0 mM), NBQX (10 μM) and TTX (1 μM). The internal recording solution contained: 130 mM $KMeSO_3$, 10 mM HEPES, 10 mM Na-phosphocreatine, 4 mM $MgCl_2$, 4 mM Na_2-ATP, 0.4 mM Na_2-GTP, 3 mM ascorbate, 250 μM Fluo-4FF, and 10 μM Alexa-594. NMDA-R current amplitudes were measured from 12 to 32 ms post-stimulus.

LTP experiments (Fig. S2) were performed in ACSF containing 4 mM Ca^{2+}, 1 mM Mg^{2+}, and 1 μM TTX. Uncaging-evoked excitatory postsynaptic currents (uEPSCs) were measured at ~ -70 mV in perforated patch voltage clamp mode to prevent washout of signaling molecules. The internal solution contained: 136.5 mM potassium gluconate, 17.5 mM KCl, 9 mM NaCl, 1 mM $MgCl_2$, 0.2 mM EGTA, 10 mM HEPES-KOH (pH 7.2). Perforated-patch electrodes (~ 4 MΩ) were back-filled with internal solution containing 0.5 mg/mL amphotericin B and front-filled with a small volume of internal solution lacking amphotericin B. Series resistances stabilized within 45 minutes of seal formation and were on average 30 ± 6 MΩ (mean ± sd). uEPSC amplitude was measured from 3 to 5 ms post-stimulus. LTP was induced by pairing depolarization to ~ 0 mV with 30 uncaging pulses (0.5 Hz) of the same magnitude and duration as for the structural plasticity experiments.

Back-propagating action potentials (bAPs; 40 APs at 83 Hz, repeated 4 times with 5 second intervals; Fig. 3F-I) were triggered in perforated patch clamp mode using brief

current injections at the soma (2 ms, 1-3 nA) (*1*). bAP experiments were performed in ACSF containing 4 mM Ca^{2+}, 1 mM Mg^{2+}, 10 μM NBQX, and 5 μM CPP.

Immunofluorescence

Hippocampal slice cultures were fixed in 4% paraformaldehyde plus 4% sucrose (in 0.1 M phosphate buffer) for 30 minutes at room temperature. Following ~ 2 hours of cryoprotection in 30% sucrose (in phosphate buffer), cryosections were prepared at a thickness of 18 μm. Cryosections were blocked in 10% goat serum with 0.1% Triton-X100 at room temperature for 3 hours and then overnight at 4º C in 10% goat serum without Triton-X100. Immunostaining was performed using the primary antibody (1:100, α-Ras mouse monoclonal, BD Biosciences) for 3 hours at room temperature (in 10% goat serum with 0.1% Triton-X100) followed by the secondary antibody (1:1000, goat α-mouse conjugated to Alexa-405, Molecular Probes) for 1.5 hours at room temperature (in 2% goat serum without Triton-X100). The immunofluorescence signal was brightest along the outer membrane of the cell (Fig. S6A, C), consistent with Ras's membrane localization. Cells over-expressing Ras showed staining patterns similar to untransfected cells, indicating that exogenous Ras, at least on a gross level, was localized similarly to endogenous Ras (Fig. S6C).

To compare mEGFP-Ras fluorescence to the immunofluorescence signal across multiple slices (Fig. S6D), the mEGFP fluorescence was normalized to the signal of green fluorescent beads (1 μm diameter) injected into the section ~ 30 μm from the soma. The fluorescent beads were monodisperse (CV = 0.09). The signals from ~ 10 beads were averaged per cell.

The immunofluorescence signal (Alexa 405) was quantified using two-photon images (780 nm excitation) and was isolated from mEGFP and mRFP fluorescence using a bandpass filter (440/80, Chroma). Multiple regions-of-interest (ROIs) were analyzed along the outer membrane of the soma and averaged following background subtraction from an ROI in the nucleus. Multiple cells were averaged for the endogenous Ras signal. The Ras over-expression level was defined as the ratio of exogenous Ras expression to endogenous Ras levels and was measured as:

$$\text{Ras over - expression level} = \frac{I_{transfected} - I_{untransfected}}{I_{untransfected}} \qquad \text{Eq. S1}$$

where I is the fluorescence intensity of the immunofluorescence signal. The immunofluorescence signal was proportional to the concentration of Ras (Fig. S6B, D). Our measurement of H-Ras over-expression may be an underestimate because the Ras antibody might also detect K- and N-Ras isoforms. However, H-Ras is the dominant isoform in the juvenile rat brain (*25, 26*). Also, the spread of Ras activation, Ras mobility, and $\tau_{inactivation}$ showed only weak relationships with expression level (Fig. 2D, 3C, 3E, 3I).

2pFLIM Data Analysis

We imaged FRET using 2pFLIM. Each pixel of a FLIM image represents the fluorescence lifetime of the donor fluorophore (mEGFP), which is defined as the average time between fluorophore excitation and photon emission. The lifetime is obtained from the fluorescence decay curve following pulsed excitation (Fig. 1B). A shorter lifetime implies higher FRET. To quantify Ras activation, we calculated the fraction of mEGFP-Ras (donor) molecules bound to mRFP-RBD(R59A)-mRFP (acceptor) molecules (binding fraction). The binding fraction can be calculated by direct fitting of the fluorescence decay curve (*F(t)*; Fig. 1B), which is composed of two populations corresponding to free donors (P_D) and donors bound to acceptors (P_{AD}; binding fraction) with fluorescence lifetimes τ_D and τ_{AD}, respectively (*1*):

$$F(t) = F_o \left[P_D \exp(-t / \tau_D) + P_{AD} \exp(-t / \tau_{AD}) \right] \qquad \text{Eq. S2}$$

In time-correlated single photon counting measurements, the fluorescence decay curve is convolved with the pulse response function (PRF) of the microscope, which is the uncertainty in the arrival times of photons mostly due to the transit time spread of the PMT (assumed to be Gaussian with width τ_G) (*1*). The fluorescence decay curve therefore can be expressed as:

$$F_{Double}(t,t_0,\tau_D,\tau_G,\tau_{AD},P_D,P_{AD}) = F_0[P_D \cdot G(t,t_0,\tau_D,\tau_G) \\ + P_{AD} \cdot G(t,t_0,\tau_{AD},\tau_G)]$$

<div align="right">Eq. S3</div>

where G is the convolution of the Gaussian PRF and an exponential decay:

$$G(t,t_0,\tau_D,\tau_G) = \frac{1}{2}\exp\left(\frac{\tau_G^2}{2\tau_D} - \frac{t-t_0}{\tau_D}\right)\mathrm{erf}\left(\frac{\tau_G^2 - \tau_D(t-t_0)}{\sqrt{2}\tau_D\tau_G}\right)$$

<div align="right">Eq. S4</div>

However, in the case of small ROIs with limited photon counts ($\sim 10^4$ photons), such as individual spines, direct fitting can be unstable. The fluorescence lifetime can also be obtained from the mean photon arrival time. The mean photon arrival time, <t>, can be measured as:

$$\langle t \rangle = \frac{\int dt \cdot t F(t)}{\int dt \cdot F(t)}$$

Ref. (*15*)

<div align="right">Eq. S5</div>

The mean photon arrival time is related to the mean fluorescence lifetime, <τ>, by an offset arrival time, t_o, that depends on the position of the sample:

$$\langle \tau \rangle = \langle t \rangle - t_o$$

Ref. (*1*)

<div align="right">Eq. S6</div>

First, we determined the offset arrival time using the full field-of-view, which has higher photon counts ($\sim 10^6$ photons). We obtained the mean photon arrival time for the full field-of-view using Eq. S5. We then calculated the fluorescence lifetime by fitting the fluorescence decay curve for the full field-of-view (Eq. S3) with two exponentials with time constants τ_D and τ_{AD}. The fit was constrained by fixing τ_D, τ_{AD}, and τ_G to values obtained in HEK293 cells ($\tau_D = 2.53$ ns, $\tau_{AD} = 1.00$ ns, and $\tau_G = 0.157$ ns) (*1*). From the fit, we calculated the mean fluorescence lifetime, where the theoretical average for multiple populations (i.e. free donors and donors bound to acceptors) is given by:

$$\langle \tau \rangle \sim \frac{\int dt \cdot t \left[(1 - P_{AD}) \cdot \exp(-t/\tau_D) + P_{AD} \cdot \exp(-t/\tau_{AD})\right]}{\int dt \cdot \left[(1 - P_{AD}) \cdot \exp(-t/\tau_D) + P_{AD} \cdot \exp(-t/\tau_{AD})\right]}$$
$$\sim \frac{(1 - P_{AD})\tau_D^2 + P_{AD}\tau_{AD}^2}{(1 - P_{AD})\tau_D + P_{AD}\tau_{AD}}$$

Eq. S7

Using Eq. S6, we determined the offset arrival time. For individual ROIs or pixels, we measured the mean photon arrival time, using Eq. S5, and then used the offset arrival time to calculate the fluorescence lifetime. The binding fraction (P_{AD}) within each ROI was obtained from Eq. S7 as:

$$P_{AD} = \frac{\tau_D(\tau_D - \langle \tau \rangle)}{(\tau_D - \tau_{AD})(\tau_D + \tau_{AD} - \langle \tau \rangle)}$$

Eq. S8

All binding fraction data and lifetime images were obtained in this manner. The binding fraction change was calculated as the mean binding fraction at 1 to 3 minutes post-stimulus minus the mean baseline binding fraction. Binding fraction changes were similar across all initial spine volumes (Fig. S11A). The decay-time constant of Ras activation was calculated as the area under the curve divided by the peak. Comparisons of the decay of Ras activity under normal conditions and during synaptic crosstalk (i.e. without and with application of the subthreshold protocol following the LTP protocol; compare Figs. 1G and 4E) were made using the difference in binding fraction between the time points before and after the subthreshold protocol (ΔBinding fraction$_{\text{without sub protocol}}$ = -0.019 ± 0.005, ΔBinding fraction$_{\text{with sub protocol}}$ = -0.016 ± 0.007, P > 0.4).

Data analysis

To estimate spine volumes, the integrated red fluorescence in the spine (from mRFP-RBD(R59A)-mRFP), which is proportional to spine volume (*27*), was normalized to the fluorescence in the thick apical dendrite (*28*). This value, multiplied by the volume of the point spread function, gives the spine volume (in units of fL $\equiv$ μm^3). The transient volume change was calculated as the mean volume at 1 to 3 minutes minus the mean volume at 15.5 to 19.5 minutes, normalized to the baseline volume. The sustained volume

change was calculated as the mean volume at 15.5 to 19.5 minutes minus the mean baseline volume, normalized to the baseline volume (Figs. 1E, S4E). Percent volume changes were weakly, negatively correlated with the initial spine volume (Fig. S11C-D). The volume increase caused by NMDA-R activation could be overestimated because a population of mRFP-RBD(R59A)-mRFP binds to activated Ras in the stimulated spine. However, since mRFP-RBD(R59A)-mRFP is expressed at higher levels than mEGFP-Ras (*1*), this effect is likely small. Also, the apparent spine volume was constant in nearby spines even though Ras activity increased to similar levels in the stimulated and nearby spines (Fig. S4B).

The origin of all time axes corresponds to the start of the uncaging train. All data are presented as mean ± sem, unless indicated otherwise. *P* values are from two-tailed *t*-tests, unless noted otherwise.

Estimation of the diffusion coefficient (D) of Ras from paGFP experiments

We assume that the spine head membrane (area *A*) is a well-mixed compartment and that diffusional exchange between the spine head and parent dendrite is limited by the narrow spine neck (length *l*, circumference *s*). Then the time constant of exchange is given by:

$$\tau = \frac{l}{s}\frac{A}{D}$$
Eq. S9

Assuming $s = 0.3$ μm, $l = 0.8$ μm, $A = 1$ μm^2, and $\tau = 4.5$ s yields $D = 0.6$ μm^2/s. This value is consistent with the estimate from the diffusion-reaction model of Ras activity and with previous direct measurements in non-neuronal cells (*29*).

Model of the spatial profile of Ras activity

We used a one-dimensional diffusion-reaction scheme to model Ras diffusion along a dendrite. The concentration of active Ras (Φ) above baseline activity is given by:

$$\frac{\partial \Phi(x,t)}{\partial t} = D\frac{\partial^2 \Phi(x,t)}{\partial x^2} - \frac{1}{\tau_{inactivation}}\Phi(x,t) \qquad \text{Eq. S10}$$

where D is the diffusion coefficient of Ras and $\tau_{inactivation}$ is the time constant of Ras inactivation. Given a point-source ($x = 0$), providing Ras activity with time course $f(t)$, Φ is given by:

$$\Phi(x,t) \sim \int_0^t d\tau \cdot H(x,t-\tau)f(\tau) \qquad \text{Eq. S11}$$

where $H(x, t)$ is:

$$H(x,t) \sim \frac{1}{\sqrt{2Dt}}\exp\left(-\frac{x^2}{2Dt} - \frac{t}{\tau_{inactivation}}\right). \qquad \text{Eq. S12}$$

We assume that the GEF activity decays with a time constant of τ_{GEF}. When the stimulus starts at $t = 0$, and ends at $t = t_0$ (1 min), $f(t)$ can be expressed as:

$$f(t) = \begin{cases} 1 - \exp(-t/\tau_{GEF}) & 0 \le t < t_0 \\ [1 - \exp(-t_0/\tau_{GEF})]\exp(-t/\tau_{GEF}) & t_0 \le t \end{cases} \qquad \text{Eq. S13}$$

We obtained D, τ_{GEF} and $\tau_{inactivation}$ by fitting our data from 2 to 7 minutes post-stimulus (Fig. 2) using a non-linear least-squares regression. In the steady state condition, Φ is given by:

$$\Phi(x) \sim \exp(-x/L) \qquad \text{Eq. S14}$$

where the space constant L is given by:

$$L = \sqrt{D\tau_{inactivation}} \qquad \text{Eq. S15}$$

Supplementary Information

Glutamate uncaging-evoked [Ca^{2+}] transients

We imaged [Ca^{2+}] transients produced by glutamate uncaging in neurons filled with a green Ca^{2+}-sensitive indicator (250 μM Fluo 4FF, *G*) and a red Ca^{2+}-insensitive dye (10 μM Alexa 594, *R*; Fig. S1). To calculate [Ca^{2+}] from fluorescence measurements, we used the relationship:

$$\frac{G/R}{(G/R)_{max}} = \frac{\left[Ca^{2+}\right]}{K_D + \left[Ca^{2+}\right]} \qquad\qquad \text{Eq. S16}$$

where $(G/R)_{max}$ is the ratio of green to red fluorescence at saturating [Ca^{2+}] and the dissociation constant, K_D, for Fluo 4FF is 10.4 μM (*30*).

Uncaging pulses produced a peak $(\Delta G/R)/(G/R)_{max}$ value of 0.36 ± 0.04 (Fig. S1C, E), corresponding to a peak [Ca^{2+}] transient of ~ 5.9 μM. This value is smaller than the [Ca^{2+}] accumulations measured during low frequency synaptic stimulation at 0 mV (~ 12 μM) (*31*) and is therefore in a physiological range.

[Ca^{2+}] transients in the stimulated spine were ~ 8 times larger than the [Ca^{2+}] signals in the parent dendrite at the mouth of the spine neck (Fig. S1C, E). In our [Ca^{2+}] imaging experiments, the [Ca^{2+}] signal spread along the dendrite up to 2 μm (Fig. S1D). Our [Ca^{2+}] measurements were performed with high concentrations of exogenous buffer. Ca^{2+} bound to the indicator is more mobile than Ca^{2+} bound to endogenous buffers (*32, 33*), and the presence of the indicator prolongs the time course of the [Ca^{2+}] transient (*31*). Therefore, the spatial spread of the [Ca^{2+}] signal is increased in [Ca^{2+}] imaging experiments (see Eq. 1). All Ras activation experiments were performed without exogenous Ca^{2+} buffer and therefore will show even greater compartmentalization of Ca^{2+}. Even in the presence of high concentrations of exogenous buffer, the spread of the [Ca^{2+}] signal was much shorter than the spread of Ras activation (compare Figs. 2B and S1D). Also, trains of uncaging stimuli (30 pulses at 0.5 Hz, 1 ms pulse duration) that

produced $[Ca^{2+}]$ accumulations ~ 2 times larger than the dendritic $[Ca^{2+}]$ signal (Fig. S1E) did not trigger Ras activation (ΔBinding fraction $= 0.004 \pm 0.006$, $P > 0.6$; Fig. S1F). We conclude that our uncaging stimuli produced physiological, compartmentalized $[Ca^{2+}]$ transients and that any spread of Ca^{2+} did not contribute to Ras activation.

Pathways to NMDA receptor-dependent Ras activation in single spines

What are the signaling pathways coupling synaptic activity and Ras activation? Although numerous studies have identified signaling factors important for ERK activation (*34*), few have examined the signaling molecules that regulate Ras activity (*35-39*). Because Ras has multiple downstream effectors (*40*) and since ERK can be activated in a Ras-independent manner (*34, 41, 42*), the regulation of Ras activity may differ from the regulation of ERK. Furthermore, the pathways coupling Ca^{2+} and Ras-ERK activity have been studied using biochemical techniques combined with global, non-physiological stimuli. In these assays it is often difficult to disentangle the contributions of different Ca^{2+} sources to Ras activation.

We therefore identified the signaling molecules that shape glutamate receptor-dependent Ras activation in dendritic spines during the induction of synaptic plasticity. Plasticity inducing stimuli (30 uncaging pulses, 0.5 Hz) at a single spine triggered robust Ras activation in the stimulated spine (ΔBinding fraction $= 0.085 \pm 0.007$, $P < 0.0001$; Fig. 1C, F-G). We measured the involvement of specific signaling pathways in the activation of Ras using pharmacological techniques. Pharmacology allows for an acute perturbation of the signaling network and does not suffer from the compensatory changes associated with molecular genetic techniques (*43-45*). To overcome the lack of specificity of pharmacological inhibitors, we used multiple drugs wherever possible. The use of glutamate uncaging to activate postsynaptic glutamate receptors bypasses possible presynaptic pharmacological effects. To ensure that changes in Ras activation reflected inhibition of downstream signaling events, rather than the modification of NMDA-Rs, we measured the uncaging-evoked NMDA-R currents in the presence of each pharmacological blocker in parallel experiments (Fig. S9).

We began by investigating the coupling of Ca^{2+} and Ras. Ras activation was abolished when extracellular Ca^{2+} was reduced 20-fold to 200 μM (ΔBinding fraction$_{\text{fraction control}}$ = 0.03 ± 0.06, $P < 0.0001$ versus control; Fig. S3D), confirming that Ras activation is Ca^{2+}-dependent. To test if NMDA-Rs are critical for Ras activation we applied the NMDA-R antagonist CPP (10 μM) and the metabotropic glutamate receptor (mGluR) antagonist MCPG (500 μM). CPP completely blocked Ras activation (ΔBinding fraction$_{\text{fraction control}}$ = 0.02 ± 0.03, $P < 0.0001$ versus control; Fig S3A-D), while MCPG had no effect (ΔBinding fraction$_{\text{fraction control}}$ = 1.02 ± 0.23, $P > 0.5$ versus control; Fig. S3D). Ras activation is therefore mediated by activation of NMDA-Rs. Under some conditions, Ras can be activated specifically by NR2A- (*39*) or NR2B- (*38*) containing NMDA-Rs. To test if Ras activity was NMDA-R subunit-dependent, we applied ifenprodil (3 μM) to block NR2B-containing receptors. Ifenprodil reduced NMDA-R currents by ~ 50% (Fig. S9) and partially blocked Ras activation (ΔBinding fraction$_{\text{fraction control}}$ = 0.39 ± 0.09, $P < 0.0001$ versus control; Fig. S3D). Reducing NMDA-R currents to a similar extent in a subunit-independent manner, by decreasing the duration of the uncaging pulse from 4 ms to 2.5 ms (Fig. S9) or by applying sub-saturating concentrations of the subunit-independent NMDA-R antagonist APV (1.5 μM), reduced Ras activation to an extent similar to ifenprodil (Reduced power: ΔBinding fraction$_{\text{fraction control}}$ = 0.43 ± 0.04, $P > 0.5$ versus ifenprodil; 1.5 μM APV: ΔBinding fraction$_{\text{fraction control}}$ = 0.46 ± 0.11, $P > 0.3$ versus ifenprodil; Fig. S3D). We conclude that under our experimental conditions Ras is activated by Ca^{2+} influx through NMDA-Rs in a subunit-independent manner.

We next explored the Ca^{2+}-dependent signals that regulate Ras activation. Calmodulin (CaM) is an abundant Ca^{2+}-dependent regulator (*46*). Application of calmidazolium (30 μM CMZ) or W7 (20 μM), which prevents the association of free CaM with its effectors, reduced Ras activation (CMZ: ΔBinding fraction$_{\text{fraction control}}$ = 0.38 ± 0.07, $P < 0.0001$ versus control; W7: ΔBinding fraction$_{\text{fraction control}}$ = 0.32 ± 0.06, $P < 0.0001$ versus control; Fig. S3D). CaMKII is a major target of CaM in spines and has been implicated in synaptic plasticity (*47*). Application of the CaMKII inhibitor KN62 (10 μM) or the myristoylated autocamtide-2 related inhibitor peptide (10 μM AIP) decreased peak Ras activation, consistent with coupling between CaMKII and Ras

(KN62: ΔBinding fraction$_{\text{fraction control}}$ = 0.73 ± 0.14, $P < 0.05$ versus control; AIP: ΔBinding fraction$_{\text{fraction control}}$ = 0.68 ± 0.18, $P < 0.07$ versus control; Fig. S3D) (*12*).

It has also been reported that nitric oxide synthase (NOS) can couple NMDA-R activation to Ras (*36*). However, application of the NOS inhibitor L-NAME (100 μM) did not change Ras activation (ΔBinding fraction$_{\text{fraction control}}$ = 1.02 ± 0.23, $P > 0.7$ versus control; Fig. S3D).

PI3K, a downstream effector of Ras, has been shown to function with Ras in a positive feedback loop (*48*) and to activate ERK (*49*). Application of the PI3K blockers LY294002 (20 μM) or wortmannin (100 nM) reduced peak Ras activity (LY294002: ΔBinding fraction$_{\text{fraction control}}$ = 0.35 ± 0.08, $P < 0.0001$ versus control; Wortmannin: ΔBinding fraction$_{\text{fraction control}}$ = 0.44 ± 0.10, $P < 0.01$ versus control; Fig. S3D). The combination of LY294002 and KN62 blocked Ras activation almost completely (ΔBinding fraction$_{\text{fraction control}}$ = 0.13 ± 0.07, $P < 0.0001$ versus control; Fig. S3D), suggesting that CaMKII and PI3K act in parallel pathways to activate Ras.

The partial block of Ras activation by calmidazolium suggests that CaM-independent pathways to Ras activation exist. Several PKC isoforms can be activated by Ca^{2+} in a CaM-independent manner through their C2 Ca^{2+}-binding domains (*50*). Application of Gö6976 (1 μM) to block specifically Ca^{2+}-dependent PKC isoforms (PKCα and PKCβ1) (*51*) decreased peak Ras activation (ΔBinding fraction$_{\text{fraction control}}$ = 0.63 ± 0.06, $P < 0.01$ versus control; Fig. S3D).

It has been suggested that ERK feeds back to activate Ras (*52*). However, in the presence of the MEK inhibitor U0126 (20 μM), which prevents ERK activation, Ras activity was unchanged (ΔBinding fraction$_{\text{fraction control}}$ = 0.87 ± 0.16, $P > 0.3$ versus control; Fig. S3D). ERK is therefore strictly downstream of Ras.

Preventing actin polymerization using latrunculin A (300 nM), which abolishes spine enlargement (see below, Fig. S4F), did not affect Ras activation

(ΔBinding fraction$_{\text{fraction control}}$ = 0.96 ± 0.21, $P > 0.7$ versus control; Fig. S3D). This suggests that signaling proteins anchored by the actin cytoskeleton may not be required for Ras activation.

We also examined the roles of the upstream activators of Ras in the spread of Ras activity. Our diffusion-reaction model and our measurements of Ras mobility (Fig. 3A-E) and $\tau_{\text{inactivation}}$ (Fig. 3F-I) suggest that the diffusion of active Ras is sufficient to account for the spread of Ras activity. However, the spread of upstream activators may also contribute through the active propagation of Ras activity. We measured the spread of Ras activity across all conditions in which signaling pathways were inhibited. The ratio of Ras activation in neighboring spines (< 4 μm from the stimulated spine) to the Ras activation in the stimulated spine was constant across all conditions (ANOVA, $P > 0.1$; Fig. S12), consistent with the passive spread of active Ras from the stimulated spine.

Ras activation therefore is controlled by multiple converging pathways, including CaMKII, PI3K, and PKC. Since PI3K is an upstream activator and downstream effector of Ras, Ras-PI3K may function in a positive feedback loop (*48*). Also, Ras activation is likely shaped by Ca^{2+}-dependent GEFs and GAPs (*35, 53-55*). Elucidating the detailed mechanisms of how these pathways couple Ca^{2+} influx to Ras activation will require the identification of the upstream activators and downstream effectors for each pathway.

Role of Ras activation in activity-dependent spine enlargement

Recent evidence indicates that LTP and LTD can be accompanied by increases (*22, 23, 56-58*) and decreases (*59*) in spine size, respectively, consistent with the observation that spine head volumes are proportional to PSD area (*60*) and AMPA-R content (*19, 61, 62*). Activity-dependent increases in spine size may be critical for synapse stabilization *in vivo* (*27*). We therefore identified the signaling molecules important for spine structural plasticity in the same set of experiments in which we dissected pathways to Ras activation.

Spines stimulated by the uncaging train (30 pulses at 0.5 Hz) grew in two distinct phases: a transient peak in spine volume ($\Delta Vol_{transient} = 110 \pm 10\%$, $P < 0.001$) decayed to a sustained spine enlargement ($\Delta Vol_{sustained} = 71 \pm 7\%$, $P < 0.001$; $\Delta Vol_{transient} + \Delta Vol_{susatined} = 181 \pm 10\%$, $P < 0.001$; Figs. 1E, S4C-E) (*22, 23*). The sustained volume change was stable from 10 to 60 minutes post-stimulus (Figs. 1E, S4E). Both phases of spine growth were larger for smaller spines (Fig. S11C-D) (*22*), but the amplitudes of transient and sustained enlargement were not correlated (Fig. S11B). Neighboring spines less than 4 µm away did not change ($\Delta Vol_{sustained} = 5 \pm 7\%$, $P > 0.4$; Fig. 1E).

Reducing the extracellular $[Ca^{2+}]$ to 200 µM abolished the spine growth ($\Delta Vol_{transient, \text{ fraction control}} = 2 \pm 9\%$, $P < 0.0001$ versus control, $\Delta Vol_{sustained, \text{ fraction control}} = -1 \pm 12\%$, $P < 0.0001$ versus control; Fig. S4F), suggesting that the structural plasticity is Ca^{2+}-dependent. Confirming earlier studies (*22*), the transient and sustained phases of spine enlargement were blocked by antagonists of NMDA-Rs (10 µM CPP: $\Delta Vol_{transient, \text{ fraction control}} = 1 \pm 5\%$, $P < 0.0001$ versus control, $\Delta Vol_{sustained, \text{ fraction control}} = 4 \pm 7\%$, $P < 0.0001$ versus control; Fig. S4F), CaM-dependent signaling (30 µM Calmidazolium: $\Delta Vol_{transient, \text{ fraction control}} = 54 \pm 9\%$, $P < 0.001$ versus control, $\Delta Vol_{sustained, \text{ fraction control}} = 23 \pm 9\%$, $P < 0.001$ versus control; Fig. S4F), and actin polymerization (300 nM Latrunculin A: $\Delta Vol_{transient, \text{ fraction control}} = 18 \pm 7\%$, $P < 0.001$ versus control, $\Delta Vol_{sustained, \text{ fraction control}} = 14 \pm 9\%$, $P < 0.001$ versus control; Fig. S4F), whereas spine growth was unaffected by a broad-spectrum blocker of mGluRs (500 µM MCPG: $\Delta Vol_{transient, \text{ fraction control}} = 109 \pm 27\%$, $P > 0.8$ versus control, $\Delta Vol_{sustained, \text{ fraction control}} = 104 \pm 19\%$, $P > 0.9$ versus control; Fig. S4F). Also, blocking Ca^{2+}-dependent PKC isoforms with Gö6976 reduced transient and sustained spine enlargement (1 µM; $\Delta Vol_{transient, \text{ fraction control}} = 70 \pm 11\%$, $P < 0.05$ versus control, $\Delta Vol_{sustained, \text{ fraction control}} = 38 \pm 13\%$, $P < 0.01$ versus control; Fig. S4F). The sustained phase, but not the transient phase, of spine enlargement was reduced by inhibiting CaMKII (10 µM KN62: $\Delta Vol_{transient, \text{ fraction control}} = 98 \pm 16\%$, $P > 0.8$ versus control, $\Delta Vol_{sustained, \text{ fraction control}} = 64 \pm 10\%$, $P < 0.01$ versus control; Fig. S4E-F) (*22*).

Is Ras signaling required for the activity-dependent spine enlargement? To test this directly we expressed a dominant negative form of FRas-F (containing the mutation Ras

S17N) to inhibit Ras signaling. Expression of Ras S17N reduced the magnitude of the sustained spine enlargement but did not affect the transient phase of spine growth ($\Delta Vol_{transient,\ fraction\ control} = 92 \pm 26\%$, $P > 0.8$ versus control, $\Delta Vol_{sustained,\ fraction\ control} = 31 \pm 18\%$, $P < 0.05$ versus control; Fig. S4F), suggesting that Ras signaling is necessary for the maintenance of spine structural plasticity. However, Ras activation was not sufficient for spine enlargement because, at the level of populations, Ras activation in stimulated and nearby spines was similar (Fig. S4B), whereas structural plasticity and LTP were synapse-specific (Figs. 1E, S2).

ERK and PI3K are key Ras effectors and both pathways have been shown to affect neuronal structure (*63, 64*). The PI3K blocker LY294002 (20 µM), which reduced peak Ras activation by ~ 60% (Fig. S3D), did not affect the induction or maintenance of the spine enlargement (20 µM LY294002: $\Delta Vol_{transient,\ fraction\ control} = 92 \pm 17\%$, $P > 0.7$ versus control, $\Delta Vol_{sustained,\ fraction\ control} = 98 \pm 19\%$, $P > 0.9$ versus control; Fig. S4F). Since Ras activity can be reduced by 60% by blocking PI3K with no effect on spine growth, 40% of total Ras activation may be sufficient for its role in maintaining spine growth. Consistently, reducing Ras activation by decreasing the NMDA-R current with reduced uncaging (2.5 ms pulse duration) did not affect the spine growth ($\Delta Vol_{transient,\ fraction\ control} = 93 \pm 14\%$, $P > 0.7$ versus control, $\Delta Vol_{sustained,\ fraction\ control} = 83 \pm 18\%$, $P > 0.5$ versus control; Fig. S4F).

A combination of PI3K and CaMKII blockers abolished the sustained phase of spine enlargement without an effect on the transient phase ($\Delta Vol_{transient,\ fraction\ control} = 88 \pm 19\%$, $P > 0.5$ versus control, $\Delta Vol_{sustained,\ fraction\ control} = 24 \pm 10\%$, $P < 0.01$ versus control; Fig. S4F). In this condition, most Ras activation is blocked (Fig. S3D), and the inhibition of spine growth is larger than the addition of each individual blocker's effect, supporting the involvement of Ras activity in the sustained spine enlargement.

In contrast to the inhibition of PI3K, application of the MEK inhibitor U0126, which prevents ERK activation, reduced the sustained volume change without affecting the transient spine enlargement (20 µM U0126: $\Delta Vol_{transient,\ fraction\ control} = 89 \pm 9\%$, $P > 0.3$

versus control, $\Delta Vol_{\text{sustained, fraction control}} = 45 \pm 10\%$, $P < 0.01$ versus control; Fig. S4C-F).
Because blocking ERK did not affect Ras activation (Fig. S3D), ERK functions
downstream of Ras and is required for the maintenance of structural plasticity.
Interestingly, combining inhibitors of CaMKII (KN62) and ERK (U0126) blocked spine
growth almost completely ($\Delta Vol_{\text{transient, fraction control}} = 117 \pm 15\%$, $P > 0.5$ versus control,
$\Delta Vol_{\text{sustained, fraction control}} = 22 \pm 11\%$, $P < 0.001$ versus control; Fig. S4E-F), suggesting
that CaMKII and ERK act in parallel to maintain spine growth.

Spine enlargement in neurons transfected with GFP showed a similar time course and
pharmacological profile to those expressing FRas-F (Fig. S10), suggesting that
expression of FRas-F does not perturb the signaling network in the spine.

Potential FRas-F-dependent effects on the spatial spread of Ras activity

The presence of the Ras sensor FRas-F requires the expression of exogenous Ras
and RBD, which could distort the spatial spread of Ras activity. Assuming the passive
spread of Ras, the mean distance active Ras travels before it is inactivated depends on the
effective diffusion coefficient of Ras, D_{eff}, and the inactivation time constant, $\tau_{\text{inactivation}}$,
such that the length constant of Ras activity is given by:

$$L \sim \sqrt{D_{\text{eff}} \tau_{\text{inactivation}}}$$ Eq. S17

High Ras concentrations may enhance D_{eff} by saturating scaffolds and could increase
$\tau_{\text{inactivation}}$ due to GAP saturation. Also, RBD competes with GAPs for binding to active
Ras, thus increasing $\tau_{\text{inactivation}}$ (*1*). We therefore modeled the effects of FRas-F expression
on D_{eff} and $\tau_{\text{inactivation}}$.

Effect of FRas-F expression on Ras mobility

We modeled the potential effects of Ras over-expression on Ras mobility due to
the saturation of scaffolds. We assumed that there is a homogeneous population of
scaffolds in the spine and that the association-dissociation cycle between Ras and

scaffolds is fast. The effective diffusion coefficient of Ras, D_{eff}, depends on the fraction of Ras bound to scaffolds:

$$D_{\text{eff}} = fD_{\text{free}} + (1-f)D_{\text{bound}} \qquad\qquad \text{Eq. S18}$$

where f is the fraction of free Ras and D_{free} and D_{bound} are the diffusion coefficients of free Ras and Ras bound to scaffolds, respectively. f can be calculated from the dissociation constant, K_{D}, between Ras and scaffolds (S) using $[\text{Ras}]_{\text{free}}$ and $[\text{S}]_{\text{free}}$:

$$K_D = \frac{[Ras]_{free}[S]_{free}}{[Ras \bullet S]} \qquad\qquad \text{Eq. S19}$$

Since

$$[Ras]_{total} = [Ras]_{free} + [Ras \bullet S] \qquad\qquad \text{Eq. S20}$$

And

$$[S]_{total} = [S]_{free} + [Ras \bullet S] \qquad\qquad \text{Eq. S21}$$

Then

$$
\begin{aligned}
f &= \frac{[Ras]_{free}}{[Ras]_{total}} \\
&= \frac{[Ras]_{total} - [S]_{total} - K_D + \sqrt{([Ras]_{total} + [S]_{total} + K_D)^2 - 4([Ras]_{total}[S]_{total})}}{2[Ras]_{total}}
\end{aligned}
\qquad \text{Eq. S22}
$$

Using Eqs. S18 and S22, we calculated D_{eff} across Ras expression levels for varying affinities (K_{D}) between Ras and scaffolds (Fig. S5A). Ras mobility increases with higher Ras concentrations. The effect is largest with strong interactions between Ras and scaffolds. Therefore if active Ras interacts strongly with immobile scaffolds in the spine,

we expect an increase in Ras mobility with higher expression levels. However, our paGFP-Ras G12V experiments revealed that the apparent mobility of active Ras did not change with expression levels (Fig. 3C, E). These data argue that active Ras does not associate strongly with immobile, or slowly mobile, scaffolds in the spine and that Ras over-expression does not greatly enhance the spatial spread of Ras activity by increasing D_{eff}.

Effects of FRas-F expression on $\tau_{inactivation}$

We next modeled the potential effects of FRas-F expression on the time course of Ras activation. The saturation of GAPs by high Ras concentrations could increase the time constant of Ras inactivation, $\tau_{inactivation}$. We assumed that there is a homogeneous population of GAPs in the spine with similar affinities for Ras. The time course of Ras activity can be obtained from Michaelis-Menten kinetics as:

$$\frac{d\left[Ras^{GTP}\right]}{dt} = \frac{-V_{max}}{1 + K_D \big/ \left[Ras^{GTP}\right]} \qquad \text{Eq. S23}$$

where K_D is the dissociation constant between active Ras and GAPs. We modeled the time course of Ras activity across Ras expression levels. When GAPs are not saturated ($[Ras^{GTP}] << K_D$), Ras inactivation is expressed as an exponential decay:

$$\left[Ras^{GTP}\right] = \left[Ras^{GTP}\right]_0 \exp\left(-\frac{K_D}{V_{max}}t\right) \qquad \text{Eq. S24}$$

When GAPs are saturated, Ras is inactivated with a constant rate (V_{max}):

$$\left[Ras^{GTP}\right] = \left[Ras^{GTP}\right]_0 - V_{max}t \qquad \text{Eq. S25}$$

Thus $\tau_{inactivation}$, which we calculated experimentally as the area divided by the peak of the decay curve (Fig. 3H-I), linearly correlates with $[Ras^{GTP}]$ (Fig. S5B):

$$\tau_{inactivation} \sim \frac{\left[Ras^{GTP}\right]}{V_{max}} \qquad \text{Eq. S26}$$

Consistently, our experimental measurements showed an approximately linear relationship between $\tau_{inactivation}$ and [Ras^{GTP}] (Fig. 3I).

The expression of RBD is also expected to enhance the duration of Ras activation. Binding between RBD and active Ras reduces the amount of free active Ras on which GAPs can act. We can calculate the concentration of free active Ras from the dissociation constant between Ras and RBD:

$$K_D = \frac{\left[RBD\right]\left[Ras^{GTP}\right]_{free}}{\left[RBD \bullet Ras^{GTP}\right]} \qquad \text{Eq. S27}$$

where K_D between Ras^{GTP} and RBD(R59A) is ~ 4 µM (*3*). Since

$$\left[Ras^{GTP}\right]_{total} = \left[Ras^{GTP}\right]_{free} + \left[RBD \bullet Ras^{GTP}\right] \qquad \text{Eq. S28}$$

Then the rate of Ras inactivation is decreased by a factor of:

$$\kappa = \frac{\left[Ras^{GTP}\right]_{free}}{\left[Ras^{GTP}\right]_{total}} = \frac{K_D}{\left[RBD\right] + K_D} \qquad \text{Eq. S29}$$

Therefore, $\tau_{inactivation}$ increases linearly with [RBD]:

$$\tau_{inactivation} = \tau_{native}\left(1 + \left[RBD\right]/K_D\right) \qquad \text{Eq. S30}$$

where τ_{native} is the inactivation time constant at [RBD] = 0 (Fig. S5C).

Consistently, our measurements of the time course of Ras activity showed a linear increase in $\tau_{\text{inactivation}}$ with higher FRas-F expression levels. We could not distinguish between the effects due to the expression of exogenous Ras and RBD. However, the linear relationship between $\tau_{\text{inactivation}}$ and FRas-F expression level allowed extrapolation to estimate $\tau_{\text{inactivation}}$ in the native case (Fig. 3I).

Estimate of the number of spines regulated by Ras following the activation of a single spine

        We have measured the spread of Ras activation after stimulation of single spines ($L \sim 11$ μm at 4 minutes post-stimulus; Nearby spines < 3 μm from the stimulated spine: ΔBinding fraction$_{\text{nearby spines}}$ = 0.061 ± 0.004, $P < 0.0001$; Fig. 2A-B). Even though Ras activity spreads over ~ 10 μm, the effective length scale of Ras-dependent signaling could be much shorter. For example, the highest levels of Ras activity, close to the stimulated spine, could be required to trigger downstream signaling. However, our data indicate that neighboring spines experience Ras activity levels sufficient for effective Ras signaling. First, at the level of spine populations, Ras activation in stimulated spines and nearby spines less than 4 μm away overlap extensively (Fig. S4B). Second, although activity-dependent spine enlargement requires Ras activity, Ras activation can be reduced by > 50% (by decreasing NMDA-R activation or blocking PI3K; Fig. S3D) without obvious effects on the spine volume increase (Fig. S4F). Approximately 50% of Ras activity is therefore sufficient for Ras's role in spine structural plasticity. Ras activation in nearby spines (less than 4 μm from the stimulated spine) is only ~ 30% lower than for the stimulated spine on average (Figs. 1G, S12). We conclude that the levels of Ras activity in neighboring spines are sufficient to trigger downstream signaling.

We estimated the number of synapses regulated by Ras following the activation of a single synapse, assuming that Ras activity levels half those in the stimulated spine are sufficient to trigger signaling events (based on Ras's role in spine structural plasticity). We calculated the length constant of Ras activity in the native case as $L \sim 6$ μm at 2 minutes after the stimulus (assuming FRas-F expression increases $\tau_{\text{inactivation}}$ by a factor of ~ 2; Figs. 2B, 3I). This length constant corresponds to a full-width at half maximum of

~ 10 µm. Since each micrometer of dendrite in CA1 pyramidal neurons contains 1-2 spines on average (*60*), Ras activity is therefore expected to regulate 10-20 spines.

The spread of Ras signaling over short stretches of dendritic length including multiple synapses may have multiple downstream effects. The spread of Ras-dependent signaling was necessary for interactions between nearby synapses due to the local modulation of the LTP induction threshold (*23*). The spread of Ras activity might also contribute to other local phenomena, such as changes in dendritic excitability (*65*), spine formation (*64*), and dendritic protein synthesis (*66*).

Supplementary References

1.   R. Yasuda *et al.*, *Nat Neurosci* **9**, 283 (2006).

2.   H. Niv, O. Gutman, Y. Kloog, Y. I. Henis, *J Cell Biol* **157**, 865 (2002).

3.   B. K. Jaitner *et al.*, *J Biol Chem* **272**, 29927 (1997).

4.   O. Rocks *et al.*, *Science* **307(5716)**, 1746 (2005).

5.   V. K. Chiu *et al.*, *Nat Cell Biol* **4**, 343 (2002).

6.   M. Fivaz, T. Meyer, *J Cell Biol* **170**, 429 (2005).

7.   H. Husi, M. A. Ward, J. S. Choudhary, W. P. Blackstock, S. G. Grant, *Nat Neurosci* **3**, 661 (2000).

8.   S. A. Kushner *et al.*, *J Neurosci* **25**, 9721 (2005).

9.   G. H. Patterson, J. Lippincott-Schwartz, *Science* **297**, 1873 (2002).

10.   V. De Paola, S. Arber, P. Caroni, *Nat Neurosci* **6**, 491 (2003).

11.   L. Stoppini, P. A. Buchs, D. A. Muller, *J. Neurosci. Methods* **37**, 173 (1991).

12.   J. J. Zhu, Y. Qin, M. Zhao, L. Van Aelst, R. Malinow, *Cell* **110**, 443 (2002).

13.   G. Feng *et al.*, *Neuron* **28**, 41 (2000).

14.   T. A. Pologruto, B. L. Sabatini, K. Svoboda, *BioMedical Engineering OnLine* **2**, 13 (2003).

15.   J. R. Lakowicz, *Principles of Fluorescence Spectroscopy* (Plenum, New York, ed. Second, 1999).

16.   Z. F. Mainen *et al.*, *Methods* **18**, 231 (1999).

17.   W. Denk, *Proc Natl Acad Sci U S A* **91**, 6629 (1994).

18.   T. Furuta *et al.*, *Proc Natl Acad Sci U S A* **96**, 1193 (1999).

19.   M. Matsuzaki *et al.*, *Nat Neurosci* **4**, 1086 (2001).

20.   A. G. Carter, B. L. Sabatini, *Neuron* **44**, 483 (2004).

21.   A. Sobczyk, V. Scheuss, K. Svoboda, *J. Neurosci.* **25**, 6037 (2005).

22.   M. Matsuzaki, N. Honkura, G. C. Ellis-Davies, H. Kasai, *Nature* **429**, 761 (2004).

23.   C. D. Harvey, K. Svoboda, *Nature* **450**, 1195 (2007).

24.   N. W. Gray, R. M. Weimer, I. Bureau, K. Svoboda, *PLoS Biol* **4** (2006).

25.   J. Leon, I. Guerrero, A. Pellicer, *Mol Cell Biol* **7**, 1535 (1987).

26.   W. Wei, S. S. Schreiber, M. Baudry, G. Tocco, D. Broek, *Brain Res Mol Brain Res* **19**, 339 (1993).

27.   A. J. Holtmaat *et al.*, *Neuron* **45**, 279 (2005).

28.   E. A. Nimchinsky, R. Yasuda, T. G. Oertner, K. Svoboda, *J Neurosci* **24**, 2054 (2004).

29.   P. H. Lommerse *et al.*, *Biophys J* **86**, 609 (2004).

30.   R. Yasuda *et al.*, *Sci STKE* **2004**, pl5 (2004).

31.   B. L. Sabatini, T. G. Oertner, K. Svoboda, *Neuron* **33**, 439 (2002).

32.   N. L. Allbritton, T. Meyer, L. Streyer, *Science* **258**, 1812 (1992).

33.   M. Gabso, E. Neher, M. E. Spira, *Neuron* **18**, 473 (1997).

34.   J. D. Sweatt, *Curr Opin Neurobiol* **14**, 311 (2004).

35.   M. B. Kennedy, H. C. Beale, H. J. Carlisle, L. R. Washburn, *Nat Rev Neurosci* **6**, 423 (2005).

36.   H. Y. Yun, M. Gonzalez-Zulueta, V. L. Dawson, T. M. Dawson, *Proc Natl Acad Sci U S A* **95**, 5773 (1998).

37.   X. Tian *et al.*, *Embo J* **23**, 1567 (2004).

38.   G. Krapivinsky *et al.*, *Neuron* **40**, 775 (2003).

39.   M. J. Kim, A. W. Dunah, Y. T. Wang, M. Sheng, *Neuron* **46**, 745 (2005).

40.   Y. Qin *et al.*, *Genes Dev* **19**, 2000 (2005).

41.   S. Mishra, S. M. Smolik, M. A. Forte, P. J. Stork, *Curr Biol* **15**, 366 (2005).

42.   Y. Obara, A. M. Horgan, P. J. Stork, *J Neurochem* **101**, 470 (2007).

43.   E. Marder, J. M. Goaillard, *Nat Rev Neurosci* **7**, 563 (2006).

44.   A. M. Swensen, B. P. Bean, *J Neurosci* **25**, 3509 (2005).

45.   E. S. Piedras-Renteria *et al.*, *Proc Natl Acad Sci U S A* **101**, 3609 (2004).

46.   Z. Xia, D. R. Storm, *Nat Rev Neurosci* **6**, 267 (2005).

47.   J. Lisman, H. Schulman, H. Cline, *Nat Rev Neurosci* **3**, 175 (2002).

48.   M. Fivaz, S. Bandara, T. Inoue, T. Meyer, *Curr Biol* **18**, 44 (2008).

49.   L. J. Chandler, G. Sutton, N. R. Dorairaj, D. Norwood, *J Biol Chem* **276**, 2627 (2001).

50.   H. Mellor, P. J. Parker, *Biochem J* **332 (Pt 2)**, 281 (1998).

51.   G. Martiny-Baron *et al.*, *J Biol Chem* **268**, 9194 (1993).

52.   U. S. Bhalla, P. T. Ram, R. Iyengar, *Science* **297(5583)**, 1018 (2002).

53.   C. L. Farnsworth *et al.*, *Nature* **376**, 524 (1995).

54.   P. J. Cullen, P. J. Lockyer, *Nat Rev Mol Cell Biol* **3**, 339 (2002).

55.   S. J. Cook, P. J. Lockyer, *Cell Calcium* **39(2)**, 101 (2006).

56.   C. Lang *et al.*, *Proc Natl Acad Sci U S A* **101**, 16665 (2004).

57.   C. D. Kopec, B. Li, W. Wei, J. Boehm, R. Malinow, *J Neurosci* **26**, 2000 (2006).

58.   C. D. Kopec, E. Real, H. W. Kessels, R. Malinow, *J Neurosci* **27**, 13706 (2007).

59.   Q. Zhou, K. J. Homma, M. M. Poo, *Neuron* **44**, 749 (2004).

60.   K. M. Harris, J. K. Stevens, *J. Neurosci.* **9**, 2982 (1989).

61.   Z. Nusser *et al.*, *Neuron* **21**, 545 (1998).

62.   Y. Takumi, V. Ramirez-Leon, P. Laake, E. Rinvik, O. P. Ottersen, *Nat Neurosci* **2**, 618 (1999).

63.   V. Kumar, M. X. Zhang, M. W. Swank, J. Kunz, G. Y. Wu, *J Neurosci* **25**, 11288 (2005).

64.   G. Y. Wu, K. Deisseroth, R. W. Tsien, *Nat Neurosci* **4**, 151 (2001).

65.   L. L. Yuan, J. P. Adams, M. Swank, J. D. Sweatt, D. Johnston, *J Neurosci* **22**, 4860 (2002).

66.   R. J. Kelleher, 3rd, A. Govindarajan, H. Y. Jung, H. Kang, S. Tonegawa, *Cell* **116**, 467 (2004).
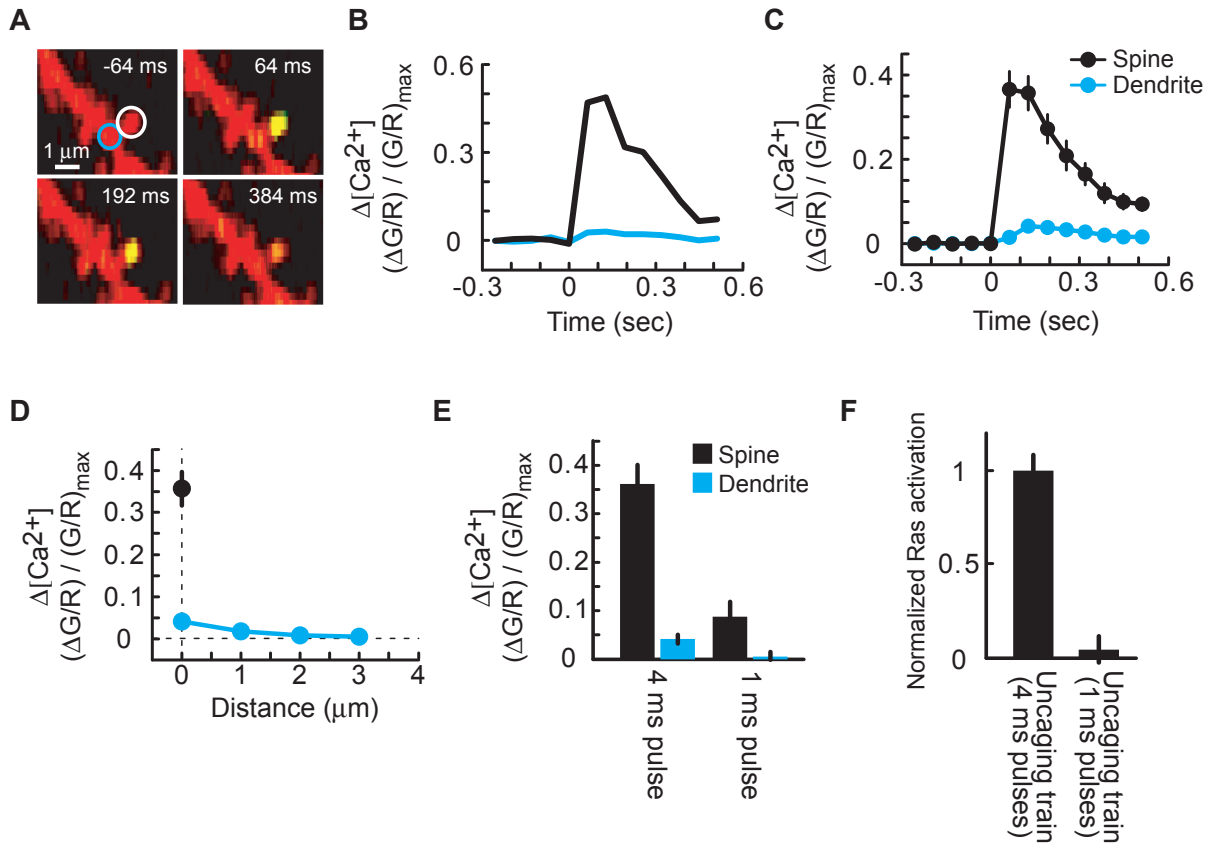
Figure S1: Glutamate uncaging-evoked $[Ca^{2+}]$ transients. **(A)** Images of a cell loaded with a green Ca^{2+}-sensitive indicator (G, 250 µM Fluo-4FF) and a red Ca^{2+}- insensitive dye (R, 10 µM Alexa-594) before and after an uncaging pulse. At time = 0, a single uncaging pulse of the same magnitude and duration (4 ms) as an individual pulse from the plasticity-inducing uncaging train was applied to the spine indicated in white in low (nominally 0 mM) extracellular Mg^{2+}. **(B)** Quantification of the $[Ca^{2+}]$ transient for the experiment shown in (A). $\Delta[Ca^{2+}]$ was calculated as the change in green fluorescence divided by the red fluorescence ($\Delta G/R$), normalized to the green-to-red ratio at saturating $[Ca^{2+}]$, $(G/R)_{max}$. The colors correspond to the ROIs in (A). **(C)** $[Ca^{2+}]$ transients in the stimulated spine and parent dendrite. n = 24 spines from 4 cells, mean ± sem. **(D)** The spatial spread of the $[Ca^{2+}]$ signal. $\Delta[Ca^{2+}]$ was measured at the indicated distances along the dendrite. Note that the addition of exogenous Ca^{2+} buffer (250 µM Fluo-4FF) increases the spatial spread of the $[Ca^{2+}]$ signal. **(E)** Peak $[Ca^{2+}]$ accumulations for 4 ms and 1 ms uncaging pulses at constant laser power (18 mW at the back focal aperture of the objective). **(F)** Ras activation in the stimulated spine following trains of uncaging stimuli (30 pulses at 0.5 Hz) with 4 ms or 1 ms pulse durations. 4 ms data are from Fig. 1. For 1 ms pulses, n = 15 spines. $P < 0.001$.
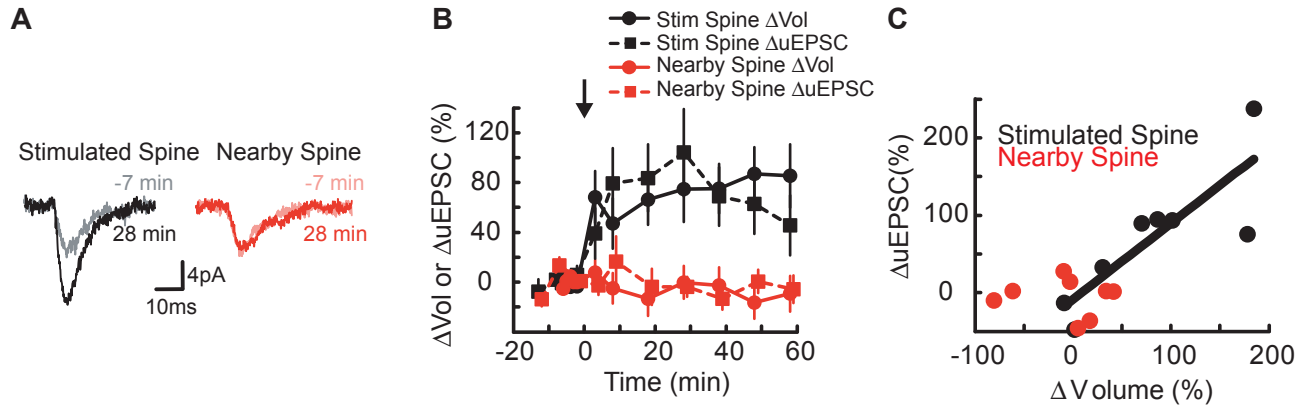
Figure S2: Relationship between structural plasticity and LTP. **(A)** Uncaging-evoked excitatory postsynaptic currents (uEPSCs) before (-7 min) and after (28 min) plasticity induction. uEPSCs were measured in perforated patch voltage clamp configuration at ~ -70 mV. At time = 0, 30 uncaging pulses (0.5 Hz) paired with depolarization to ~ 0 mV were applied to a single spine (stimulated spine) in 4 mM Ca^{2+} and 1 mM Mg^{2+}. Following the pairing protocol, uEPSCs were enhanced at the stimulated spine (black) but not at the nearby spine (red). Traces are the averages of 6 trials. **(B)** Time course of changes in uEPSC amplitudes and spine volumes for the stimulated and nearby spines. $n = 8$, mean ± sem. **(C)** Changes in uEPSC amplitude and spine volume for individual stimulated and nearby spines. For the stimulated spine, $r = 0.83$, $P < 0.01$.
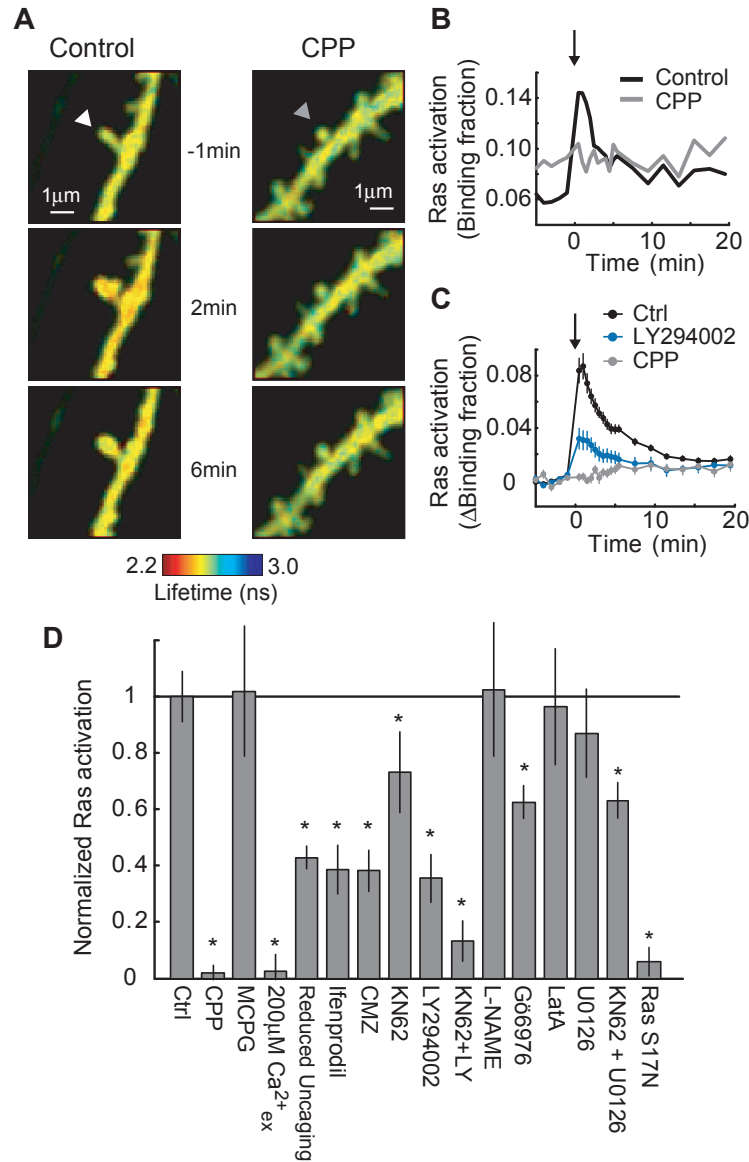
Figure S3: NMDA receptor-dependent pathways to Ras activation. **(A)** Fluorescence lifetime images before and after uncaging trains in control and CPP (10 μM) conditions. At time = 0, 30 uncaging pulses (0.5 Hz) were applied to the spine marked by the arrowhead in low (nominally 0 mM) extracellular Mg^{2+}. **(B)** Ras activation in the stimulated spine for the experiments shown in (A). **(C)** Time course of Ras activation in stimulated spines. Number of spines: 82 control (data from Fig. 1), 20 LY294002 (20 μM), 12 CPP (10 μM), mean ± sem. **(D)** Pharmacological analysis of Ras activation in the stimulated spine. ΔBinding fraction was measured in the indicated conditions and normalized to the control condition. Asterisks indictate $P < 0.05$ versus control. Number of spines: 82 Ctrl, 12 CPP, 9 MCPG, 11 200 μM Ca^{2+}, 13 Reduced uncaging, 14 Ifenprodil, 21 Calmidazolium (CMZ), 27 KN62, 20 LY294002, 12 KN62 + LY294002, 10 L-NAME, 23 Gö6976, 10 Latrunculin A, 22 U0126, 12 KN62 + U0126, 11 Ras S17N. ≤ 3 spines were used from a single cell. Error bars indicate mean ± sem.
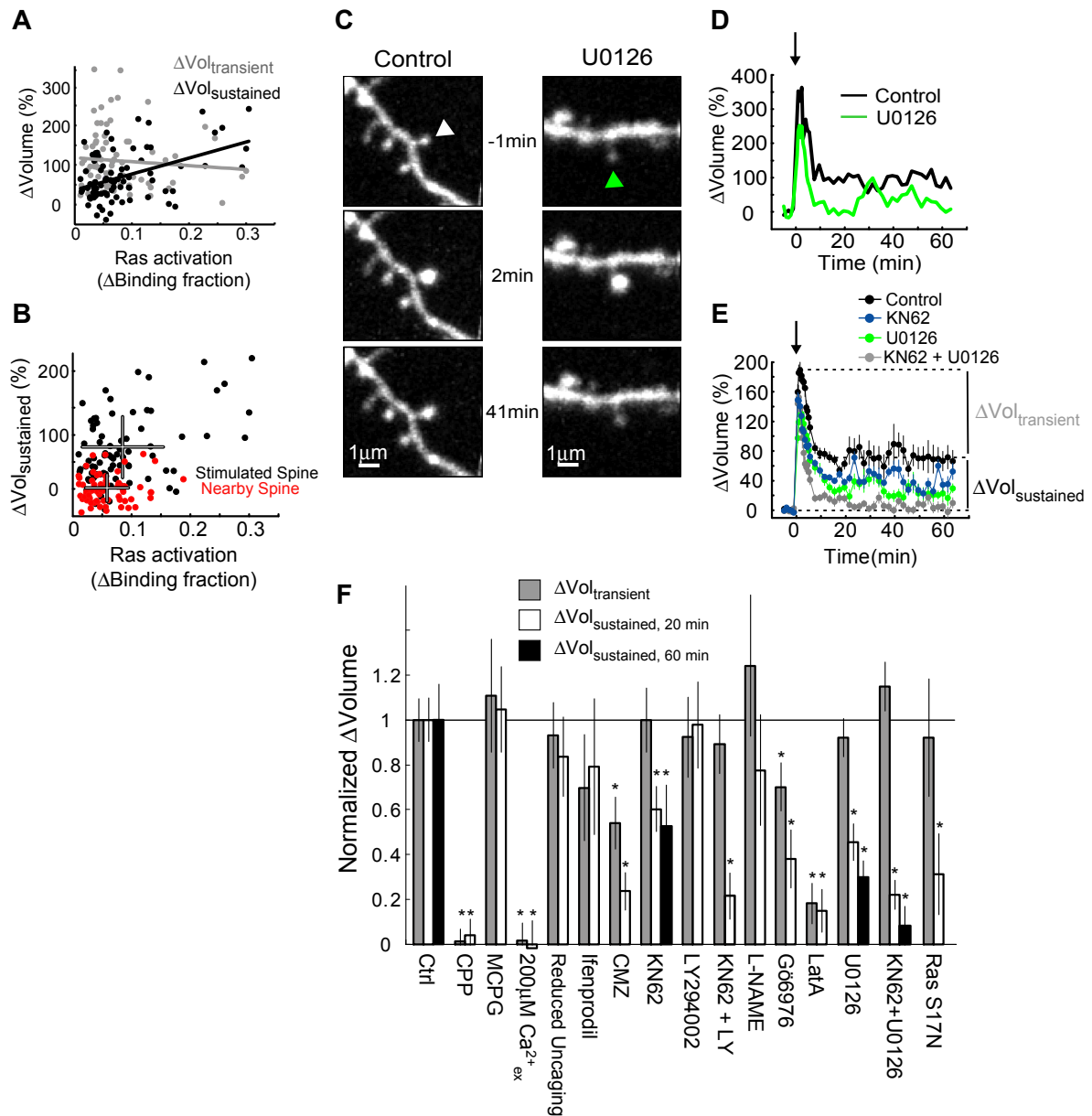
Figure S4: Role of Ras activation in activity-dependent spine enlargement. **(A)** Ras activation and volume changes for individual spines ($n = 82$). Ras activation was calculated as the average binding fraction at 1 to 3 minutes minus the baseline binding fraction. $\Delta Vol_{transient}$: $r = -0.08$, $P > 0.5$. $\Delta Vol_{sustained}$: $r = 0.45$, $P < 0.0001$. **(B)** Ras activation and sustained volume changes for the stimulated and nearby spines ($n = 82$). Crosses indicate mean ± sd. **(C)** Red fluorescence (mRFP-RBD(R59A)-mRFP) images from FRas-F-expressing cells before and after uncaging trains in the control condition and in the presence of the MEK blocker U0126. At time = 0, 30 uncaging pulses (0.5 Hz) were applied to the spine marked by the arrowhead in low (nominally 0 mM) extracellular

Mg^{2+}. **(D)** Spine volume changes for the stimulated spine in the experiments from (C). **(E)** Time course of volume changes for stimulated spines. For 0 to 20 minutes, number of spines: 91 control (data are from Fig. 1), 34 KN62 (10 μM), 31 U0126 (20 μM), 22 KN62 + U0126. For time > 20 minutes, number of spines: 9 control, 7 KN62, 9 U0126, 12 KN62 + U0126. **(F)** Pharmacological analysis of spine volume changes. Volume changes were measured in the indicated conditions and normalized to the control condition. Asterisks indicate $P < 0.05$ versus control. Number of spines are the same as for Fig. S3D ($\Delta Vol_{transient}$ and $\Delta Vol_{sustained}$, 20 min) and Fig. S4E ($\Delta Vol_{sustained}$, 60 min). Error bars indicate mean ± sem.

A

Ras-Scaffold Interaction

B

Ras-GAP Interaction
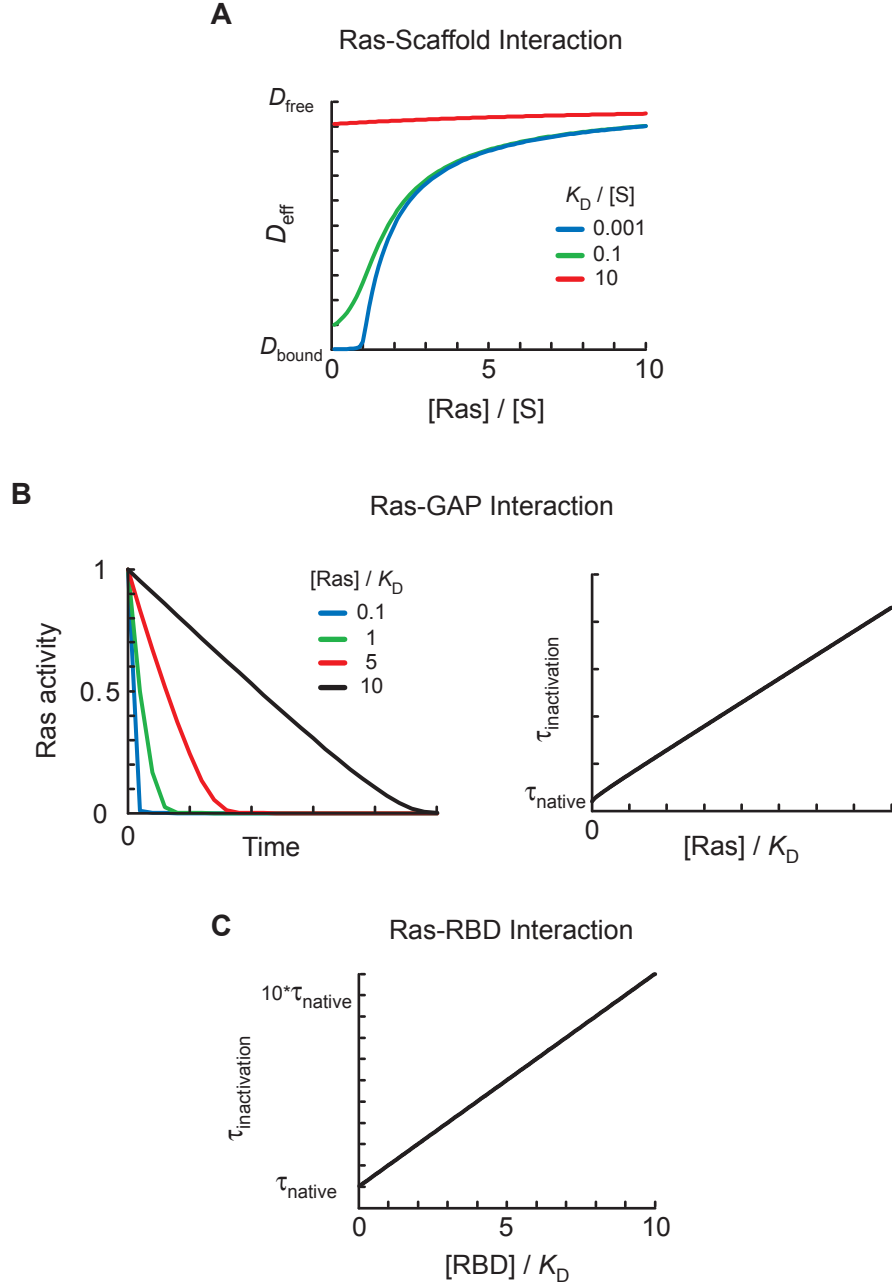
C

Ras-RBD Interaction

Figure S5: Potential effects of FRas-F expression on Ras mobility and the time constant of Ras inactivation. **(A)** Effect of Ras expression levels on the effective diffusion coefficient of Ras (D_{eff}), based on a model of Ras-scaffold interactions. If Ras interacts strongly with scaffolds in the spine, D_{eff} is expected to increase with expression levels due to the saturation of binding sites. However, if Ras interacts weakly with scaffolds, then D_{eff} is relatively independent of Ras expression levels. **(B)** Effect of Ras expression levels on $\tau_{inactivation}$ due to the saturation of GAPs, based on a model of Ras-GAP interactions. Left, the time course of Ras activity at varying Ras levels. Right, $\tau_{inactivation}$ is expected to increase approximately linearly with Ras expression level. **(C)** Effect of RBD expression on $\tau_{inactivation}$ due to competition between RBD and GAPs for binding to active Ras, based on a model of Ras-RBD interactions. $\tau_{inactivation}$ is expected to be linearly related to [RBD].
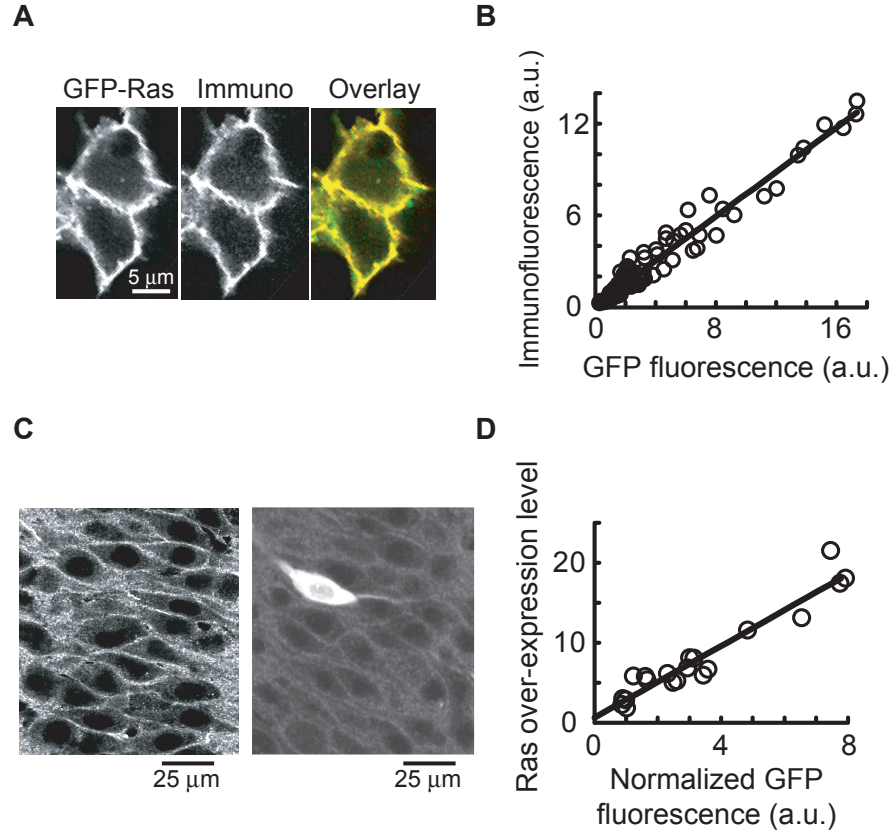
Figure S6: Linearity of the Ras immunofluorescence signal. **(A)** GFP fluorescence and immunofluorescence images of HEK293 cells transfected with mEGFP-Ras. The cells were stained with an α-Ras antibody and an Alexa-405-conjugated secondary antibody. In the overlay image, the GFP fluorescence and the immunofluorescence are pseudo-colored green and red, respectively. **(B)** Correlation between the Ras immunofluorescence signal and mEGFP fluorescence in HEK293 cells transfected with mEGFP-Ras. Signals were quantified at the plasma membrane. Each point represents an individual cell ($n = 78$ cells). Data are from an individual dish. $r = 0.98$, $P < 0.0001$. A second dish showed similar results ($r = 0.92$, $P < 0.0001$). **(C)** Immunofluorescence images of α-Ras staining in cryosections of cultured hippocampal slices. Left, endogenous Ras staining. Notice the bright staining along the plasma membrane. Right, staining of a transfected and untransfected cells. **(D)** Correlation between mEGFP fluorescence and the Ras over-expression level determined by immunofluorescence in hippocampal pyramidal neurons transfected with mEGFP-Ras. Ras over-expression was measured as the ratio of exogenous to endogenous Ras. The mEGFP fluorescence was normalized to the signal from fluorescent beads injected into the slice near the soma. Signals were quantified at the outer membrane of the soma. $n = 20$ cells. $r = 0.96$, $P < 0.0001$.
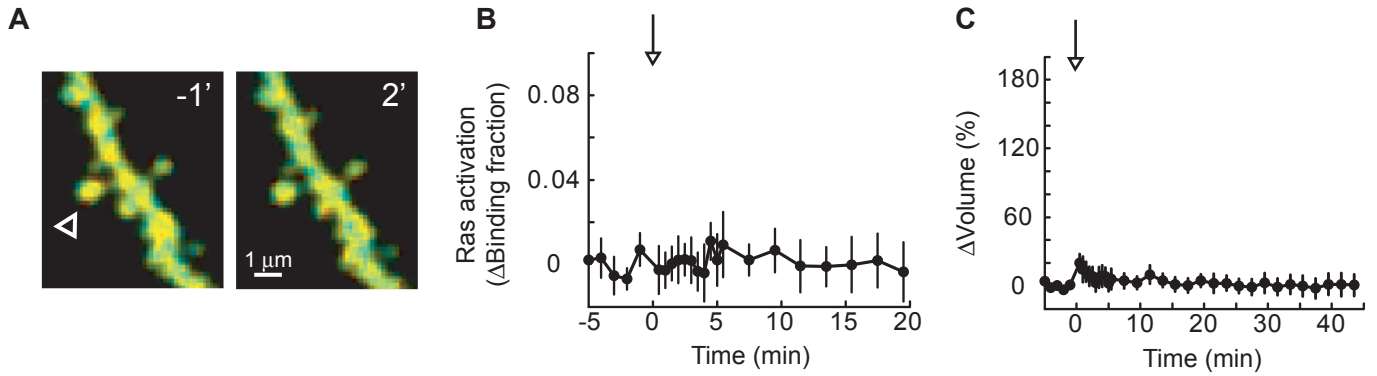
A -1' 2' 1 μm

B Ras activation (ΔBinding fraction) vs Time (min)

C ΔVolume (%) vs Time (min)

Figure S7: Measurement of Ras activation following the subthreshold protocol. **(A)** Fluorescence lifetime images before (-1 min) and after (2 min) the subthreshold uncaging protocol. At time = 0, 30 uncaging pulses (0.5 Hz, 1 ms pulse duration) were applied to the spine marked by an arrowhead in low (nominally 0 mM) extracellular Mg^{2+}. **(B)** Ras activation in the stimulated spine following the subthreshold protocol (15 spines, mean ± sem). **(C)** Spine volume changes in the stimulated spine following the subthreshold protocol (15 spines, mean ± sem).
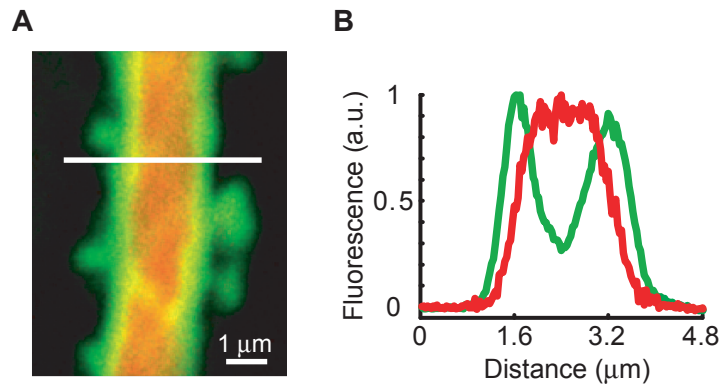
A

B

1 µm

Figure S8: Membrane localization of mEGFP-Ras. **(A)** Green and red fluorescence image of the thick apical dendrite of a cell transfected with FRas-F (mEGFP-Ras and mRFP-RBD(R59A)-mRFP). **(B)** Green and red fluorescence measured along the white line in (A).
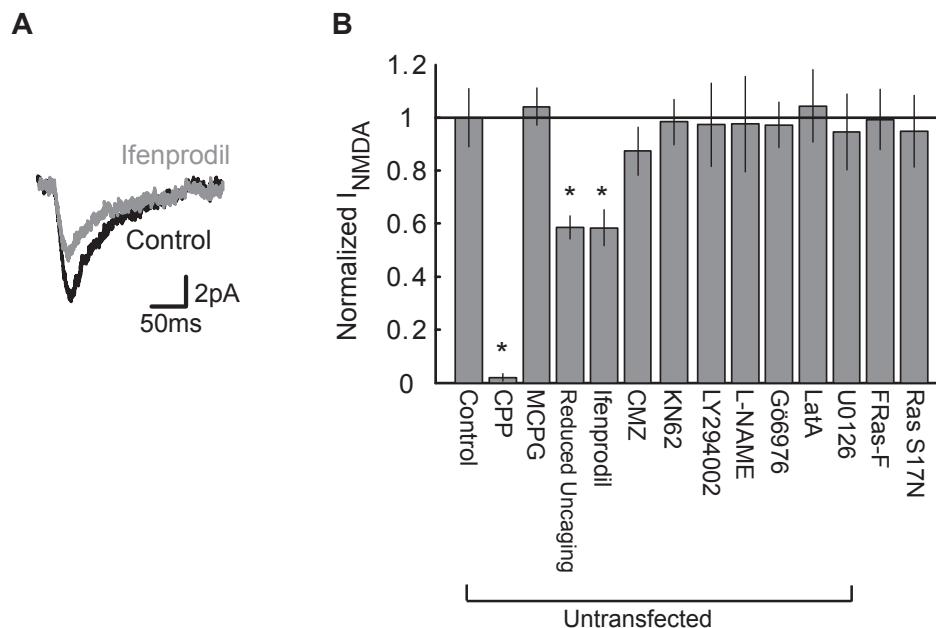
Figure S9: Glutamate uncaging-evoked NMDA receptor currents. **(A)** NMDA-R-mediated currents in the control condition and in the presence of 3 μM ifenprodil. Uncaging-evoked currents were measured at ~ -70 mV in voltage clamp in the absence of extracellular Mg^{2+} and in the presence of 10 μM NBQX. The magnitude and duration (4 ms) of the uncaging pulse was the same as for individual pulses from the uncaging train. Currents are averaged for all spines in the condition. **(B)** NMDA-R-mediated currents in the presence of pharmacological blockers, normalized to the control condition. For each condition, data are from more than 15 spines from at least 3 cells. Error bars indicate mean ± sem. Asterisks indicate $P < 0.05$ versus control.
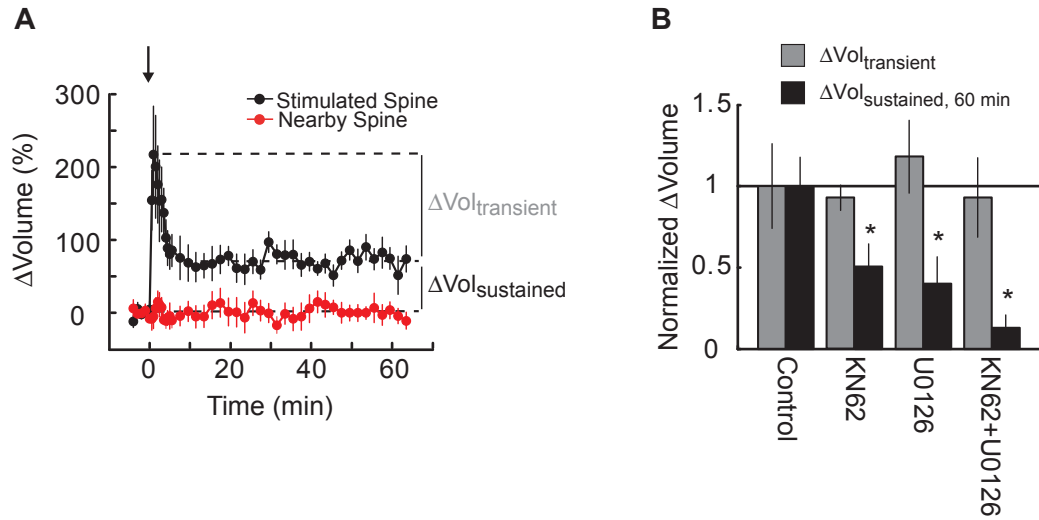
Figure S10: Spine structural plasticity in GFP-expressing neurons. **(A)** Time course of spine enlargement in the stimulated and nearby spines. At time = 0, 30 uncaging pulses (0.5 Hz) were applied to the stimulated spine in low (nominally 0 mM) extracellular Mg^{2+}. Nearby spines were less than 4 μm from the stimulated spine on the same dendritic branch. The experimental conditions were identical to those used for FRas-F experiments (e.g. Figs. 1, S4). $n = 6$, mean ± sem. **(B)** Pharmacological analysis of spine enlargement. Volume changes were measured in the indicated conditions and normalized to the control condition. Number of spines: 6 control, 8 KN62 (10 μM), 6 U0126 (20 μM), 6 KN62 + U0126. Error bars indicate mean ± sem. Asterisks indicate $P < 0.05$ versus control.
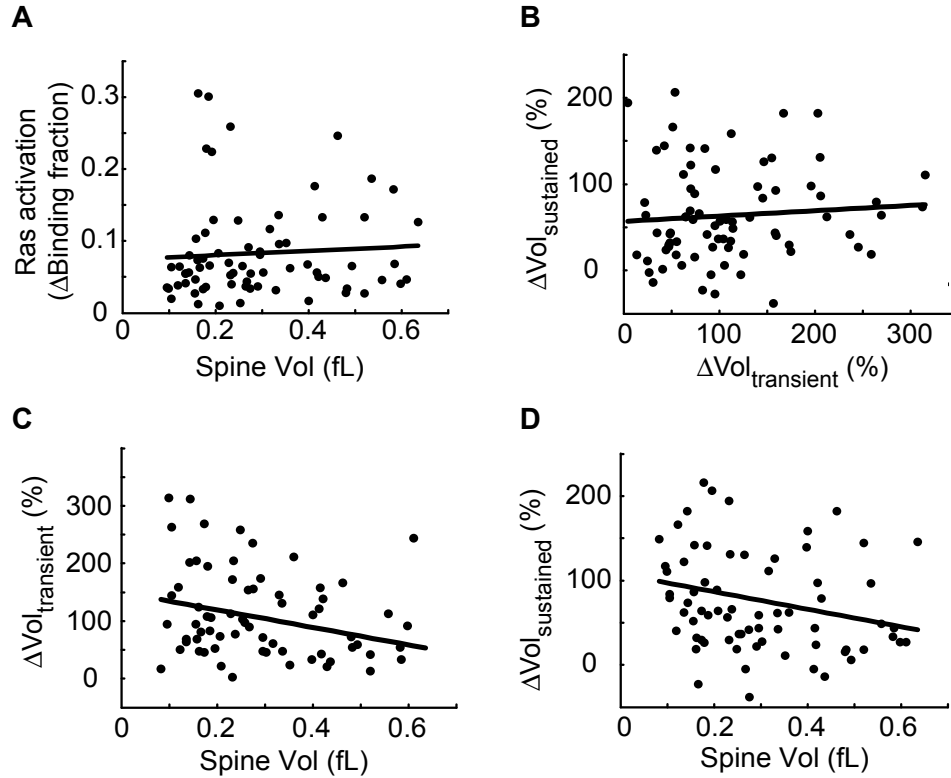
Figure S11: Relationships between Ras activation, volume changes, and initial spine volumes for stimulated spines in the control condition. **(A)** Ras activation and initial spine volumes for individual spines. $r = 0.06$, $P > 0.5$. **(B)** Transient and sustained volume changes for individual spines. $r = -0.03$, $P > 0.5$. **(C)** Transient volume changes and initial spine volumes for individual spines. $r = 0.28$, $P < 0.03$. **(D)** Sustained volume changes and initial spine volumes for individual spines. $r = 0.24$, $P = 0.06$.
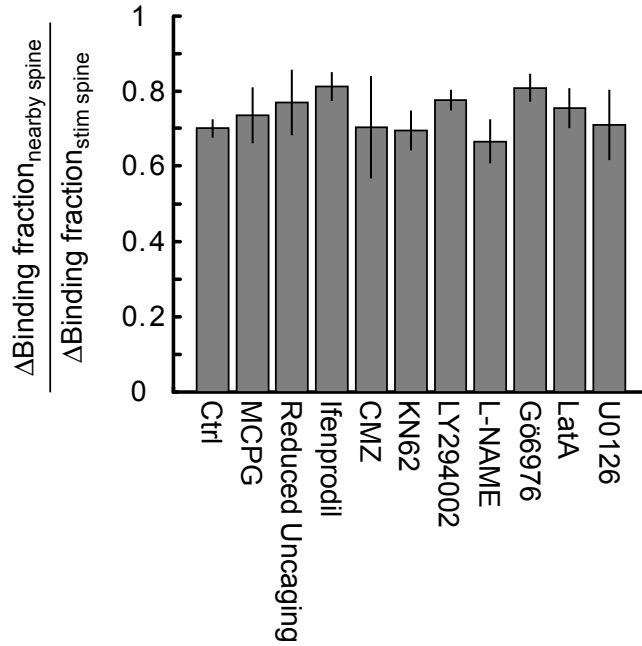
Figure S12: Spread of Ras activity in the presence of pharmacological inhibitors. The spread of Ras activity was measured as the ratio of the binding fraction change in a nearby spine to the change in the stimulated spine. Nearby spines were less than 4 μm from the stimulated spine. The mean distances between spines did not differ significantly across conditions. The number of spines were the same as for Fig. S3D.